

OPENNAVMAP: Structure-Free Topometric Mapping via Large-Scale Collaborative Localization

Jianhao Jiao¹, Changkun Liu², Jingwen Yu³, Boyi Liu³, Qianyi Zhang⁴, Yue Wang⁵, Dimitrios Kanoulas^{1,6}

arXiv:2601.12291v1 [cs.RO] 18 Jan 2026

Abstract—Scalable and maintainable map representations are fundamental to enabling large-scale visual navigation and facilitating the deployment of robots in real-world environments. While collaborative localization across multi-session mapping enhances efficiency, traditional structure-based methods struggle with high maintenance costs and fail in feature-less environments or under significant viewpoint changes typical of crowd-sourced data. To address this, we propose OPENNAVMAP, a lightweight, structure-free topometric system leveraging 3D geometric foundation models for on-demand reconstruction. Our method unifies dynamic programming-based sequence matching, geometric verification, and confidence-calibrated optimization to robust, coarse-to-fine submap alignment without requiring pre-built 3D models. Evaluations on the Map-Free benchmark demonstrate superior accuracy over structure-from-motion and regression baselines, achieving an average translation error of 0.62m. Furthermore, the system maintains global consistency across 15km of multi-session data with an absolute trajectory error below 3m for map merging. Finally, we validate practical utility through 12 successful autonomous image-goal navigation tasks on simulated and physical robots. Code and datasets will be publicly available.¹

Index Terms—Autonomous Navigation, Visual Localization, Collaborative Localization

I. INTRODUCTION

A. Motivation

Collaborative localization, which enables distributed agents to aggregate environmental observations across independent sessions, is fundamental to scaling visual navigation (VNav). The central challenge remains robust data association: globally aligning data across diverse viewpoints and temporal conditions. Conventional collaborative approaches typically rely on structure-based mapping pipelines that necessitate rigorous data collection, feature matching, triangulation, and global bundle adjustment [1]. However, they often lack robustness

¹Robot Perception and Learning Lab, Intelligent Robotics, Department of Computer Science, University College London, Gower Street, WC1E 6BT, London, UK. {ucacjji, d.kanoulas}@ucl.ac.uk.

²Department of Computer Science and Engineering, Hong Kong University of Science and Technology, Hong Kong, China.

³Department of Electronic and Computer Engineering, Hong Kong University of Science and Technology, Hong Kong, China.

⁴Institute of Robotics and Automatic Information System, Nankai University, Tianjin, China.

⁵College of control science and engineering, Zhejiang University, Hangzhou, China.

⁶AI Centre, Department of Computer Science, University College London, Gower Street, WC1E 6BT, London, UK and Archimedes/Athena RC, Greece.

This work was supported by the UKRI Future Leaders Fellowship [MR/V025333/1] (RoboHike). For the purpose of Open Access, the author has applied a CC BY public copyright license to any Author Accepted Manuscript version arising from this submission.

¹https://rpl-cs-ucl.github.io/OpenNavMap_page

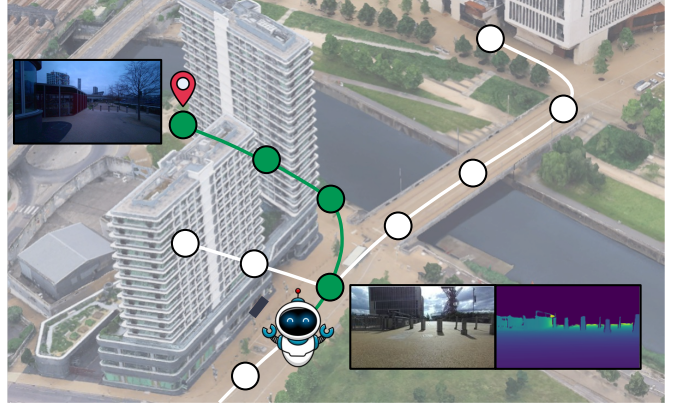


Fig. 1. Conceptual illustration of the structure-free topometric map generated by our approach, highlighting the traversability layer. During deployment, the robot utilizes RGB-D sensing to traverse the graph derived from multi-session mapping. Green nodes denote the computed shortest path to the goal image, while white nodes represent the global network of traversable locations.

in feature-sparse environments or under significant viewpoint changes [2]. Furthermore, the computational and memory costs of maintaining consistent metric maps scale prohibitively, creating a bottleneck for true lifelong autonomy.

Motivated by map-free relocalization [2], we introduce a collaborative localization approach that eliminates the need for pre-built 3D maps. We leverage feed-forward 3D geometric foundation models (GFM) [3]–[5] to infer scene geometry and camera parameters on-demand, effectively bypassing fragile classical pipelines. This shifts the paradigm away from optimizing explicit and large-scale 3D structures, and instead focuses on direct relative pose estimation using only images. Consequently, we propose a sparse, structure-free topometric map as our backbone. This lightweight, graph-based representation significantly reduces maintenance complexity, facilitating the efficient updates necessary for lifelong operation.

B. Challenges

Constructing multi-session maps presents two distinct challenges: integrating heterogeneous, uncalibrated data and achieving robust localization under dynamic conditions.

1) *Scalable Mapping Data Acquisition*: While integrating multiple sessions enhances mapping efficiency, traditional approaches are constrained by metric accuracy requirements. They typically rely on specialized hardware (e.g., high-resolution LiDARs [6]), careful calibration [7], and expert-dependent workflows [8], which significantly restrict scalability. The rise of crowd-sourced mapping via consumer devices [2], [9] enables broad data contribution such as egocentric

videos but introduces issues: 1) *Coarse Accuracy*: early initiatives such as OpenStreetMap (OSM) [10] and Google Street View [11] have shown the feasibility of scalable data aggregation but prioritized global coverage. This often results in low positional accuracy (typically 3-5m [12]), whereas robots demand sub-meter precision for reliable navigation, particularly in GNSS-denied environments. 2) *Data Variance*: Crowd-sourced data originates from diverse sensor configurations with varying intrinsics. Furthermore, uncontrolled collection introduces inconsistent image quality, such as motion blur and occlusions. These discrepancies create a substantial domain gap when associating data across devices.

2) *Collaborative Localization*: Robust data association is critical for collaborative localization but becomes challenging as maps grow in physical scale and temporal duration. This is compounded in crowd-sourced scenarios where uncontrolled trajectories often result in sparse overlap between sessions. Consequently, a system must ensure [13]: 1) *Spatial Scalability*: Robust performance across diverse environments (e.g., indoors to outdoors) by effectively handling large viewpoint variations and feature sparsity. 2) *Temporal Adaptability*: Resilience to environmental dynamics, such as moving objects and illumination changes (e.g., day-to-night), which degrade correspondences over time.

C. Contributions

This paper introduces OPENNAVMAP, a multi-session mapping system designed for scalable VNav in diverse environments. The term “*Open*” reflects our vision for a collaborative mapping paradigm, inspired by platforms such as OSM where crowd-sourced data aggregation enables dynamic and extensible maps. We employ a unified, structure-free topometric representation [14]–[16] comprising three layers: odometry, covisibility, and traversability. This architecture supports sub-meter localization and planning without relying on prior 3D environment models. While our approach leverages components such as state-of-the-art (SoTA) 3D GFMs [3] and mature SLAM-enabled products [17], our primary contribution lies in the novel system architecture that integrates and improves these components to address the challenges of large-scale, collaborative localization and map merging. Overall, OPENNAVMAP presents these key *contributions*:

- 1) **Hierarchical Collaborative Localization**: We present a three-step collaborative localization pipeline that globally registers multiple disconnected mapping sessions without prior alignment or depth data. This approach systematically integrates and improves topological localization by leveraging image sequences, metric localization with confidence map calibration for solving fine-grained poses of the query, and pose graph optimization (PGO) to enforce global consistency and smoothing (see Sec. IV-B).
- 2) **Cross-Device Localization and Mapping**: We propose several strategies to support RGB-centric cross-device localization and mapping across heterogeneous mobile platforms. By adapting to variable intrinsics and mitigating perceptual degradation, our approach resolves acquisition bottlenecks and significantly enhances mapping coverage through cross-device data collection (see Sec. IV-C).

3) **Node Culling for Lifelong Operation**: We propose a map maintenance approach designed for lifelong operation. This mechanism balances active map expansion with conservative node culling, effectively culling redundant or outdated nodes while preserving structural integrity over long-term deployments (see Sec. IV-D).

To our knowledge, OPENNAVMAP is the first system to successfully combine multi-session mapping with a structure-free topometric map explicitly designed for metric-level VNav. Its flexible design allows for seamless integration with evolving VPR models and 3D GFMs, ensuring longevity alongside algorithmic advancements. We rigorously validate the system across four distinct real-world environments, including laboratories, campuses, shopping centers, and vineyards, utilizing a dataset captured via heterogeneous devices that covers 19km and spans several months. Our results demonstrate superior accuracy, outperforming SoTA SfM and regression-based methods on the Map-Free dataset with an average translation error of 0.62m. Furthermore, the system maintains robust global consistency across 15.7km of multi-session data, achieving an ATE below 3m without using depth sensors (Table IV). Finally, we substantiate the practical utility of the map through the successful completion of 12 autonomous image-goal VNav tasks on both simulated and real robots, as demonstrated in Fig. 1. We will publicly release our code and datasets to support the community.

D. Organization

The rest of this paper is organized as follows. Sec. II reviews the relevant literature. We begin with a system overview in Sec. III. Sec. IV presents our core methodology, detailing preliminary concepts (Sec. IV-A), collaborative localization (Sec. IV-B), cross-device extensions (Sec. IV-C), and map merging with node culling and edge updating (Sec. IV-D). The VNav system utilizing the proposed topometric map is described in Sec. V. Finally, we cover the experimental setup in Sec. VI, report results in Sec. VII, provide a discussion in Sec. VIII, and conclude in Sec. IX.

II. RELATED WORK

This section briefly reviews the literature on mapping for VNav and vision-based localization for multi-session mapping.

A. Map Representations for Visual Navigation

Mapping is the process of constructing a symbolic model of the environment using sensor data and processing techniques [18]. Existing maps can generally be classified into structure-based, structure-free, and hybrid categories based on how they encode geometry.

Structure-based Maps aim to represent 3D environmental details with 3D geometric primitives such as landmarks [19] and point clouds [20]. While newer methods such as 3D Gaussians [21] reduce storage, these maps are fundamentally bound by the need to enforce global metric accuracy, making them prone to error accumulation. **Structure-free Maps** prioritize compactness through abstract representations, such as topological maps for connectivity [22], appearance-based topological

maps for visual place recognition (VPR) [23] and navigation [24], or topometric maps [14] annotated with spatial positions. This efficiency comes at the expense of explicit 3D geometry, thus limiting fine-grained localization and planning. Implicit representations such as neural radiance fields (NeRF) [25] or scene coordinate regression (SCR) [26], while extremely compact, suffer from poor interpretability and high training overhead. Moreover, these methods often require conversion to explicit geometric forms for downstream tasks [27].

Hybrid Maps combine the complementary strengths of structure-based and structure-free maps to balance metric accuracy and storage efficiency. A common approach involves building explicit structure-based maps along with corresponding topometric maps derived from navigable free space, using the former for detailed navigation and the latter for efficient planning [6]. More complex hierarchical representations, such as scene graphs [15], [28], [29], organize metric-semantic information across multiple layers, enabling efficient management of object- and room-level graphs. Several hybrid approaches prioritize local metric consistency by constructing topometric graphs that retain local geometric details only (*e.g.*, 3D landmarks [16]). This paradigm serves as the basis for systems including Visual Teach-and-Repeat (VT&R) [16], [30] and experience-based navigation [31].

Unlike standard hybrid maps that store explicit local geometry, OPENNAVMAP maintains a lightweight topometric structure composed of 2D snapshots, but augments it with a 3D GFM [3]. This integration allows for on-demand dense scene reconstruction by leveraging implicit, generalizable 3D knowledge, effectively overcoming the metric limitations of structure-free maps without the storage overhead of explicit structure-based methods. Built upon a topometric map, our VNav system introduces a Premapping-and-Navigation process that evolves the traditional Visual Teach-and-Repeat (VT&R) paradigm. In the *Premapping* phase, we replace labor-intensive manual data collection with a scalable, collaborative mapping strategy using in-the-wild mobile devices. In the *Navigation* phase, rather than relying on brittle direct visual tracking, we employ a real-time depth-based motion planning. This ensures reliable navigation even in the presence of substantial viewpoint variations and dynamic obstacles.

B. Visual Localization for Multi-Session Mapping

Visual localization (VLoc), which registers a query camera to a reference map, provides the spatial alignment necessary for collaborative localization. We classify existing literature into two categories: hierarchical and direct methods.

Hierarchical Methods operate in two stages: *topological localization* to identify corresponding places across sessions, followed by *metric localization* to compute precise camera poses. The topological stage commonly relies on VPR, employing global image representations such as Bag-of-Words [32] or learned descriptors like NetVLAD [33]. Sequence-based methods [34]–[36] further improve robustness to perceptual aliasing [37] by utilizing temporal coherence across consecutive images, though they require careful tuning of hyper-parameters such as the sequence length. The subsequent stage typically

involves explicit, structure-based maps to perform feature-based geometric refinement [1], [38], [39], often realized through Perspective-n-Point (PnP) algorithms [40] combined with RANSAC [41]. Alternatively, map-free relocalization approaches have been proposed, utilizing depth prediction with PnP or employing RAFT-based backbones to couple optical flow prediction with novel differentiable solvers [42]. Such hierarchical frameworks, which estimate the pose in a coarse-to-fine manner, currently dominate multi-session mapping research [39], [43], [44].

Direct Methods bypass an explicit topological localization stage and instead attempt to solve for the final 6-DoF metric pose directly. Typical approaches include SCR [26], which predicts the 3D world coordinates corresponding to 2D query pixels (from which a pose is then solved), and Absolute Pose Regression (APR) [45], which directly regresses the camera pose in a single feed-forward pass. However, both approaches require training a scene-specific model and are generally insufficiently robust or accurate for large-scale scenes [46], especially when compared to the precision offered by hierarchical pipelines.

Cross-Device Localization facilitates collaboration among heterogeneous robots [47]–[49]. However, variations in motion patterns, viewpoints, and modalities pose significant challenges to existing learning-based models. The CroCoDL benchmark [49] quantified these limitations and highlighted failures under drastic viewpoint changes, while 360Loc [50] specifically examined perspective-to-omnidirectional alignment. Recently, cross-modal matchers like XoFTR [51] and MatchAnything [52] have addressed these gaps, demonstrating the effectiveness of large-scale pre-training.

OPENNAVMAP advances the standard hierarchical localization framework by refining both stages. First, for topological localization, OPENNAVMAP exploits sequential constraints. It employs dynamic programming for sequence matching to increase VPR recall, complemented by a verification module that actively filters false positives. Second, regarding metric localization, OPENNAVMAP replaces pre-stored geometry with on-demand scene reconstruction. This enables a global optimization of local structure and camera poses, where residual-based confidence calibration [53] is applied to refine accuracy and reject unreliable predictions.

III. SYSTEM OVERVIEW

Fig. 2 illustrates OPENNAVMAP, a scalable multi-session topometric mapping system through large-scale collaborative localization. The pipeline aligns disconnected submaps from diverse sources into a unified global frame via three collaborative localization stages: inter-submap topological matching, geometric verification (GV), metric localization of matched node pairs, and PGO for global consistency and smoothing. The system also supports cross-device operation by adapting to variable intrinsics and perceptual degradation. To ensure lifelong scalability, the proposed probabilistic node culling regulates map growth. The resulting map enables vision-only image-goal navigation in GNSS-denied environments, allowing robots to autonomously navigate to query targets.

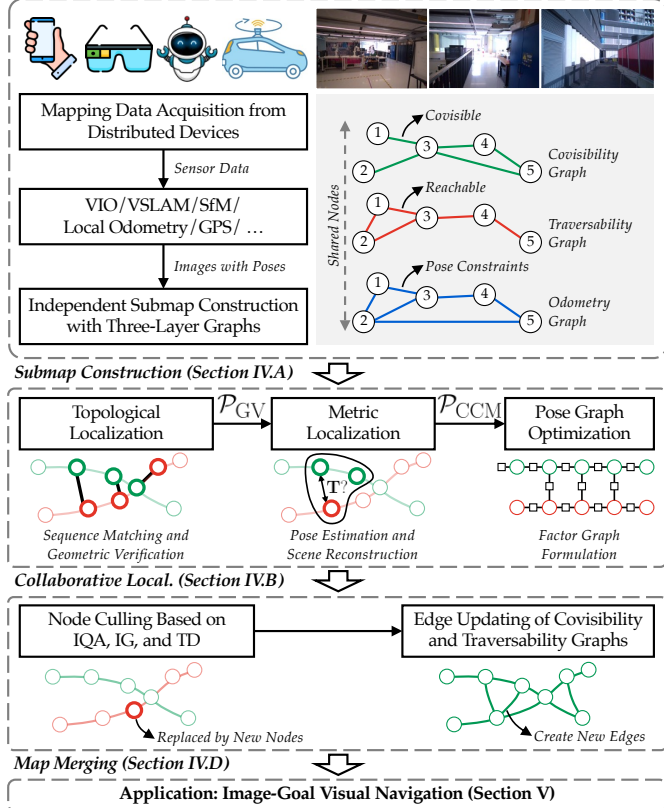


Fig. 2. Block diagram illustrating the pipeline of the proposed OPENNAVMAP system. The system builds on the topometric map with multiple layers for different utilities: covisibility, traversability, and odometry. a) Individual disconnected submaps are constructed from data collected from various devices. b) The collaborative localization consists of two steps to compute the relative transformation between the reference and query map, and then perform the PGO to jointly estimate their transformation. c) The map merging and updating module fuses these two maps by pruning data with litter information contribution and augment the connectivity of edges to update the map. d) The resulting topometric map is deployed for image-goal navigation.

IV. METHODOLOGY

This section outlines the methodology. We first introduce key preliminary concepts in Section IV-A. Section IV-B details our novel three-stage collaborative localization approach. Section IV-C presents our extensions for cross-device localization. Section IV-D presents our map merging strategy for lifelong operation, with focus on node culling and edge updating.

A. Preliminary

1) *Map Representation*: We represent the scene with a topometric map as $\mathcal{M}^W = \{\mathcal{G}_C^W, \mathcal{G}_O^W, \mathcal{G}_T^W\}$, defined entirely within the global world frame $\{\cdot\}^W$. As illustrated in Fig. 2, this map is modeled as a unified structure built upon three distinct but interrelated layers: the **Covisibility Graph** (**CvG**) – \mathcal{G}_C^W , the **Odometry Graph** (**OdG**) – \mathcal{G}_O^W , and the **Traversability Graph** (**TrG**) – \mathcal{G}_T^W . This multi-layered design serves as a unified backbone, supporting several essential functions for VNav, including localization, scene geometry recovery, and path planning. Each graph layer is an undirected graph $\mathcal{G} = \{\mathcal{N}, \mathcal{E}\}$, where \mathcal{N} is the set of nodes and \mathcal{E} is the set of edges depicting nodes' relationships. The core node set for the entire map $\mathcal{N}_C^W = \{\mathbf{n}_{C_i}^W\}_{i=1}^N$ is adopted from the

CvG, with N representing the node number. The other two graph layers share this node set. Only CvG nodes contain the rich, detailed attributes required for visual processing, such as images. Nodes in OdG and TrG utilize only the pose attributes of the shared node set. Each CvG node $\mathbf{n}_{C_i}^W$ stores the following attributes during the data acquisition session:

- **Visual Data**: The RGB image ($\mathbf{I}_i \in \mathbb{R}^{w \times h \times 3}$), its associated VPR descriptor ($\mathbf{d}_i \in \mathbb{R}^d$), and its captured timestamp ($\tau_i \in \mathbb{R}^+$).
- **Pose Information**: The globally consistent pose ($\mathbf{T}_i^W \in SE(3)$) of the node w.r.t. the world.
- **Quality Metric**: An image quality assessment (IQA) score ($q_i \in [0, 100]$) used for node culling.

The distinction between the map layers lies in the definition and function of their edges, which encode the geometric and topological relationships required for specific downstream tasks: the CvG supports VLoc, with its edges encoding the covisibility strength ($v_{C_{ij}} \in \mathbb{R}^+$) between nodes; the OdG functions as a factor graph explicitly designed for PGO, where its edges encode the relative transformation and covariance ($\mathbf{T}_{ij}, \Sigma_{ij}$), derived from either local odometry data or relative pose estimation (see Sec. IV-B); and the TrG is used for path planning, with its edges storing traversability costs ($v_{T_{ij}} \in \mathbb{R}^+$) that reflect motion feasibility. It is critical to note that the connectivity across these layers is independent: two nodes may be co-visible (CvG edge) and share pose constraints (OdG edge), but still be non-traversable (no TrG edge) if an obstacle obstructs their direct path.

2) *Submap Construction from Distributed Devices*: Individual devices generate such maps after the data capture. These submaps are further merged into a unified global map through collaborative localization, as explained in Section IV-B. We assume each device employs visual-inertial measurement units (IMUs) to provide scale-aware and locally consistent pose estimation. This capability is aligned with contemporary mobile computing platforms, such as smartphones (e.g., ARKit on iPhones) and AR glasses [17], and extends to customized robotic systems equipped with multi-sensor SLAM solutions [20], GPS-enabled 360° cameras (e.g., Insta360), and ground vehicles utilizing wheel encoders [48]. Overall, the diversity of these sources enable high-efficiency map growth across both spatial and temporal scales, supporting several general data-collection paradigms: 1) single-agent or multi-agent SfM and SLAM pipelines; 2) robots employing proprioceptive odometry based on internal sensors; and 3) geo-referenced image repositories, such as Google Street View [11].

3) *Geometric Foundation Models for Stereo Reconstruction*: Our system utilizes the MAST3R [3] network $f_{\theta}(\cdot)$, which is one of the 3D GFM, to perform the stereo reconstruction. This network processes pairs of uncalibrated RGB images $\mathbf{I}_1, \mathbf{I}_2 \in \mathbb{R}^{w \times h \times 3}$ and directly predicts normalized pointmaps $\mathbf{X}^{1,1}, \mathbf{X}^{2,1} \in \mathbb{R}^{w \times h \times 3}$, along with per-pixel confidence estimates $\mathbf{C}^{1,1}, \mathbf{C}^{2,1} \in \mathbb{R}^{w \times h \times 1}$. The reconstruction process is formally given by:

$$(\mathbf{X}^{1,1}, \mathbf{C}^{1,1}), (\mathbf{X}^{2,1}, \mathbf{C}^{2,1}) = f_{\theta}(\mathbf{I}_1, \mathbf{I}_2), \quad (1)$$

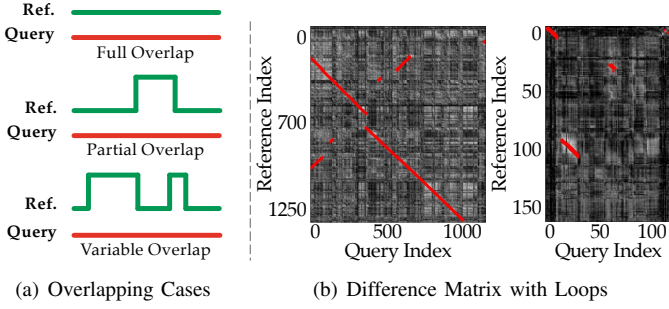


Fig. 3. Three types of trajectories occurring in multi-session mapping, with difference matrices for the latter two cases in (a). Red dots mark matched loops. The first matrix (Oxford RobotCar [7]) shows substantial overlaps, while the second (our dataset; see Sec. VI-B) exhibits sparser, irregular overlaps, highlighting the need for flexible loop closure methods.

where both pointmaps are defined in the coordinate frame of I_1 . The prediction of the confidence map is commonly used to measure the reliability of the predicted pointmaps, which is trained along with the pointmaps. Based on these outputs, we explicitly infer camera intrinsics, relative pose, and 2D feature correspondences. These intermediate results are then used for metric pose estimation, as detailed in Sections IV-B2.

B. Collaborative Localization

The objective of collaborative localization is to align multiple, independently constructed submaps into a single, globally consistent reference frame. This process is centralized where devices upload their local maps (\mathcal{M}^Q) to a server, which then iteratively integrates \mathcal{M}^Q into the existing global map (\mathcal{M}^R), yielding a progressively unified map ($\mathcal{M}^{R'}$). The OdG of each submap is formalized as a probabilistic factor graph. Within a submap, nodes are connected by intra-submap odometry factors, each encoding relative pose constraints ($\mathbf{T}_{R_j}^{R_i}, \Sigma_{R_j}^{R_i}$) between local poses. To merge two submaps into a unified global map, it is necessary to establish inter-submap edges, referred to as loop-closure factors, which encode the relative pose constraints ($\mathbf{T}_{Q_j}^{R_i}, \Sigma_{Q_j}^{R_i}$) between nodes in different submaps. Estimating these loop-closure factors, as mentioned in Sec. II-B, is accomplished through two steps. First, topological localization identifies candidate node pairs ($\mathbf{n}_i^R, \mathbf{n}_j^Q$) from different submaps that are geographically close and visually similar; and Second, metric localization estimates the precise 6-DoF relative transformations ($\mathbf{T}_{Q_j}^{R_i}, \Sigma_{Q_j}^{R_i}$).

1) *Topological Localization*: Vision-based topological localization becomes increasingly challenging as spatio-temporal scales expand: larger environments expand the search space and possibility for perceptual aliasing, while temporal gaps introduce appearance variations that heighten ambiguity. A desirable approach must achieve high precision by rejecting incorrect matches and high recall by retaining correct ones, even in perceptually challenging areas. To this end, our method consists of three steps: place descriptor extraction, sequence-based matching, and GV.

First, we extract a discriminative global **Place Descriptor** (a high-dimensional vector) for each image using a pre-trained VPR model. Based on the assumption that geographically close images are visually similar, the cosine similarity of their descriptors is used to quantify place matches.

Algorithm 1 DP-based Sequential Matching

```

1: Input: Difference matrix  $\mathbf{Diff} \in \mathbb{R}^{N \times M}$ 
2: Velocity set  $\mathbb{V} = \{V_{min}, \dots, V_{max}\}$ 
3: Jump threshold  $\Delta$ ; Penalty  $\lambda$ 
4: Output: Accumulated cost matrix  $\mathbf{C} \in \mathbb{R}^{N \times M}$ 
5: Initialize  $\mathbf{C}(i, j) \leftarrow \infty, \forall i, j; \triangleright i: \text{reference index}; j: \text{query index}$ 
6: Set  $\mathbf{C}(i, 1) = \mathbf{Diff}(i, 1)$ 
7: Set  $\mathcal{Q} \leftarrow \{(i, 1) \mid i = 1, \dots, N\}$ 
8: for  $j = 2$  to  $M$  do
9:    $\mathcal{Q}' \leftarrow \emptyset$ 
10:  for each  $(i, V) \in \mathcal{Q}$  do
11:     $i' \leftarrow i - V$   $\triangleright$  In-sequence matching
12:    if  $i' \geq 1$  and  $\mathbf{C}(i, j - 1) + \mathbf{Diff}(i', j) < \mathbf{C}(i', j)$  then
13:       $\mathbf{C}(i', j) \leftarrow \mathbf{C}(i, j - 1) + \mathbf{Diff}(i', j); \mathcal{Q}' \leftarrow \mathcal{Q}' \cup \{(i', V)\}$ 
14:    end if
15:    for  $k \in [1, i - \Delta] \cup [i + \Delta, N]$  do  $\triangleright$  Out-of-sequence jumping
16:       $Cost \leftarrow \mathbf{C}(i, j - 1) + \mathbf{Diff}(k, j) + \lambda$ 
17:      if  $Cost < \mathbf{C}(k, j)$  then
18:         $\mathbf{C}(k, j) \leftarrow Cost; \mathcal{Q}' \leftarrow \mathcal{Q}' \cup \{(k, V') \mid V' \in \mathbb{V}\}$ 
19:      end if
20:    end for
21:  end for
22:   $\mathcal{Q} \leftarrow \mathcal{Q}'$ 
23: end for

```

Single-frame descriptor matching is fragile, suffering from limited descriptor discriminability, appearance changes, and perceptual aliasing, which lead to false positives. To mitigate this, we utilize the idea of **Sequence-Based Matching** to enforce temporal consistency and improve recall. However, traditional methods such as SeqSLAM [34] rely on assumptions of continuous, overlapping trajectories and near one-to-one alignments. These assumptions do not hold in crowd-sourced scenarios which commonly feature as few sequence overlaps as well as non-contiguous matches across the reference map. Fig. 3 illustrates this problem. We formulate the sequence-based matching as a shortest-path search in a difference matrix $\mathbf{Diff} \in \mathbb{R}^{N \times M}$, where $\mathbf{Diff}(i, j)$ is the cosine distance between reference descriptor \mathbf{d}_{R_i} and query descriptor \mathbf{d}_{Q_j} . We propose a dynamic programming (DP) method to find the optimal path. Our path expansion allows two operations ($[i, j] \rightarrow [i + k, j + 1]$): 1) *in-sequence matching* ($k = V$) for continuous segments, and 2) *out-of-sequence jumping* ($|k| = \Delta$) to transition between segments. This flexibility robustly handles trajectory discontinuities. We maintain an accumulated cost matrix $\mathbf{C}(i, j)$, updated via:

$$\begin{aligned} \mathbf{C}(i, j) &\leftarrow \min[\mathbf{C}(i, j), \\ &\quad \mathbf{C}(i - V, j - 1) + \mathbf{Diff}(i, j), \\ &\quad \mathbf{C}(i - \Delta, j - 1) + \mathbf{Diff}(i, j) + \lambda], \end{aligned} \quad (2)$$

where λ is a penalty for jump operations.

Alg. 1 summarizes this method. The DP algorithm yields a set of matched reference-query node pairs, denoted as $\mathcal{P}_{\text{SM}} = \{(\mathbf{n}_i^R, \mathbf{n}_j^Q)\}$. This is retrieved by tracing back from the minimum cost in the final column $\mathbf{C}(:, M)$. However, this matching does not guarantee the precision of individual pairs. Therefore, we introduce a **GV** module to reject false positives [54]. The GV module validates keypoint matches between a reference and query image pair using RANSAC to robustly estimate a fundamental matrix. A pair is considered a true match and added to the final set \mathcal{P}_{GV} only if the number of RANSAC-inlier correspondences exceeds a threshold.

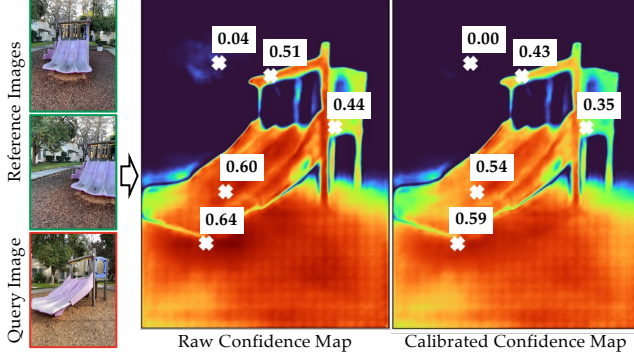


Fig. 4. The raw and calibrated confidence maps of the query image are shown after solving the optimization problem (6). Confidence values are lower in regions not covered by reference images. These values are reweighted based on the residual error, resulting in a greater reduction in low-confidence regions (e.g., 0.44 → 0.35) compared to high-confidence regions (e.g., 0.64 → 0.59).

2) *Metric Localization*: We recover the 6-DoF relative transformation for each query image from the verified node pair in \mathcal{P}_{GV} . However, the sparse, structure-free topometric map presents two key issues: 1) sparse nodes often have limited visual overlap, and 2) the lack of 3D structure, which typically serves as a strong prior in pose estimation [55].

To address this, we leverage the 3D GFM called MAS3R [3] to predict dense pointmaps. For a given reference-query pair $(\mathbf{n}_{C_i}^R, \mathbf{n}_{C_j}^Q)$, we retrieve additional reference nodes from \mathcal{G}_C^R that share high covisibility with $\mathbf{n}_{C_i}^R$. We then obtain the fine-grained query pose by globally optimizing the local scene geometry and all involved camera poses, which is given initial predictions of pointmaps, camera poses, and scale factors as input. The optimization also integrates confidence map calibration. Accuracy improves when incorporating more reference nodes, albeit at a higher computational cost. As shown in Sec. VII-B, even with few references, our method outperforms prevalent SfM-based approaches.

Global Optimization: As detailed in Sec. IV-A3, the underlying network [3] predicts pairwise 3D pointmaps, confidence maps, camera intrinsics, and relative poses between two input images. We apply this process $f_{\theta}(\mathbf{I}_i, \mathbf{I}_j)$ to all pairs where $(\mathbf{I}_i, \mathbf{I}_j) \in \mathcal{I} \times \mathcal{I}$ and $\mathcal{I} = \{\mathbf{I}_1^R, \dots, \mathbf{I}_{N-1}^R, \mathbf{I}^Q\}$ is the set of $N-1$ reference images and the query image. This constructs a connectivity graph $\mathcal{G}(\mathcal{V}, \mathcal{E})$, where vertices \mathcal{V} are image nodes and edges \mathcal{E} represent pairs with sufficient visual overlap which is measured using the confidence map. However, these pairwise predictions often lack global consistency due to factors such as varying mutual overlap and image quality; for instance, the reconstruction quality of the same scene can vary significantly between different pairs. We address this by formulating a global optimization problem to achieve consistent reconstruction and pose estimates.

We initialize the optimization by extracting the highest-confidence spanning tree from \mathcal{G} . This tree is used to propagate pairwise estimates and establish a unified global coordinate frame, providing initial values for the focal lengths $\{f_i | i = 1, \dots, N\}$, scale factors $\{\sigma^{(i,j)} \in \mathbb{R}^3\}$, and all poses $\{\mathbf{T}^{(i,j)} \in SE(3)\}$. The reference image poses $\{\mathbf{T}_i^R\}$ are considered known and are held fixed, while the query pose \mathbf{T}^Q (along with other geometric parameters) is optimized. These

parameters are refined by minimizing a 3D-3D alignment error between a unified global pointmap χ and the transformed pairwise predicted pointmaps \mathbf{X} :

$$\mathbf{T}^{Q*}, \{\chi, \sigma\}^* = \arg \min_{\mathbf{T}^Q, \{\chi, \sigma\}} \sum_{(i,j) \in \mathcal{E}} \sum_{v \in (i,j)} \sum_{p=1}^{hw} \mathbf{C}_p^{v,i} \|\chi_p^v - \sigma^{(i,j)} \mathbf{T}^{(i,j)} \mathbf{X}_p^{v,i}\|, \quad (3)$$

where $\mathbf{C}_p^{v,i}$ is the confidence map and the global pointmap χ is re-parameterized via depth back-projection:

$$\chi_p^v = \mathbf{T}_v \mathbf{K}_v^{-1} \mathbf{D}_{v,p} [u_p, v_p, 1]^\top = \mathbf{T}_v \frac{\mathbf{D}_{v,p}}{f_v} [u'_p, v'_p, 1]^\top, \quad (4)$$

where \mathbf{K}_v and \mathbf{T}_v represent the intrinsics and extrinsics for view v , and $\mathbf{D}_{v,p}$ is the depth value for pixel p . The objective in Eq. (3) can therefore be reformulated as:

$$\mathbf{T}^{Q*}, \{\mathbf{D}, f, \sigma\}^* = \arg \min_{\mathbf{T}^Q, \{\mathbf{D}, f, \sigma\}} \sum_{(i,j)} \sum_v \sum_p \mathbf{C}_p^{v,i} \|\mathbf{T}_v \frac{\mathbf{D}_{v,p}}{f_v} [u'_p, v'_p, 1]^\top - \sigma^{(i,j)} \mathbf{T}^{(i,j)} \mathbf{X}_p^{v,i}\|. \quad (5)$$

Here, the pairwise relative pose $\mathbf{T}^{(i,j)}$ and the global pose \mathbf{T}_i are parameterized independently to provide greater flexibility during optimization. The optimization is performed using several hundred iterations of gradient descent and converges within seconds on a standard GPU, yielding the optimized query pose \mathbf{T}^{Q*} . In experiments of map merging, we only use two reference images to accelerate the optimization process. This formulation (5) exhibits two valuable properties. Notably, scale-aware pointmaps and camera intrinsics are recovered as a byproduct, enabling consistent local scene reconstruction. Furthermore, the estimation quality of the pointmaps, poses, and scales is interdependent; this correlation allows us to leverage reconstruction reliability to assess pose quality.

Confidence Map Calibration: The initial confidence maps from the network's feed-forward pass are often overconfident [53], assigning high confidences to pointmaps that are in poor predictions. This may adversely affect the optimization in Eq. (5). We improve the optimization by performing confidence map calibration at each iteration, which dynamically links the confidence to the actual per-point residual. Specifically, we employ the Geman-McClure robust kernel to down-weight outliers, reformulating the objective as an iterative re-weighted least squares (IRLS) problem:

$$\mathbf{T}^{Q*}, \{\mathbf{D}, f, \sigma\}^* = \arg \min_{\mathbf{T}_Q, \{\mathbf{D}, f, \sigma\}} \sum_{(i,j)} \sum_v \sum_p \mathbf{W}_p^{v,i} \|\mathbf{e}_p^{v,i}\|, \quad (6)$$

$$\mathbf{W}_p^{v,i} = \frac{\mathbf{C}_p^{v,i}}{(1 + \|\mathbf{e}_p^{v,i}\|/\mu)^2},$$

where μ is a hyperparameter that controls outlier rejection (a smaller value provides stronger inhibition). The term $\|\mathbf{e}_p^{v,i}\|$ denotes the per-point residual: $\|\mathbf{T}_v \frac{\mathbf{D}_{v,p}}{f_v} [u'_p, v'_p, 1]^\top - \sigma^{(i,j)} \mathbf{T}^{(i,j)} \mathbf{X}_p^{v,i}\|$.

As observed from (6), pose estimation quality is inherently correlated with reconstruction quality. This relationship can be captured by the calibrated confidence map (CCM) from the final optimization iteration. Leveraging this property, we

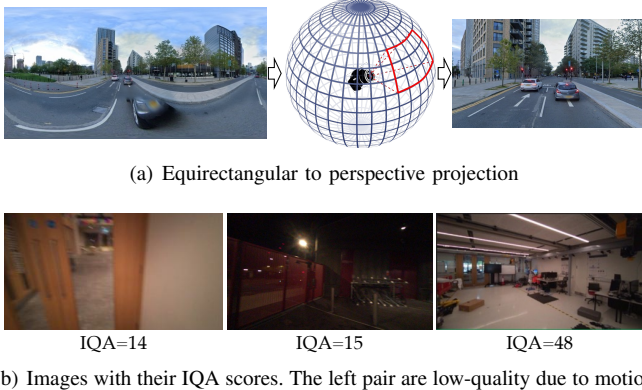


Fig. 5. Illustration of strategies for cross-device localization. (a) shows how a panoramic equirectangular image, prevalent in databases such as Google Street View, is converted into a synthetic perspective image. This transformation generates a virtual pinhole view with a user-defined FoV and camera intrinsics. (b) shows that the IQA score can quantitatively evaluate quality of an images.

use the mean of the CCM as an indicator of pose accuracy and to define an approximate covariance matrix for the pose: $\Sigma_{Q_j}^{R_i} = \text{diag}[(\bar{\mathbf{W}}_{i,i} \cdot \bar{\mathbf{W}}_{i,j})^{-2}]$. In Sec. IV-B, we leverage this confidence score to select high-confidence node pairs \mathcal{P}_{CCM} as reliable loop closure factors, effectively filtering outliers to a subsequent PGO.

3) *Pose Graph Optimization*: The preceding procedure provides high-confidence loop closure factors that link the query and reference submaps. We then construct a unified factor graph to solve a global PGO problem, jointly optimizing for: 1) submap poses in the global frame, and 2) cumulative odometry drift correction via external loop constraints, thereby ensuring the geometric consistency of the final merged map. The PGO is formulated as a robust nonlinear least-squares problem, optimizing all poses $\mathcal{T} = \{\mathbf{T}^R\} \cup \{\mathbf{T}^Q\}$ includes both reference and query poses:

$$\mathcal{T}^* = \arg \min_{\mathcal{T}} \sum_{(i,j) \in \mathcal{E}} \rho \left(\|\log[(\bar{\mathbf{T}}_j^i)^{-1}(\mathbf{T}_i)^{-1}\mathbf{T}_j]\|_{\Sigma_j^i}^2 \right), \quad (7)$$

where \mathcal{E} is the set of all factors, including odometry edges and inter-map loop closure edges; $\bar{\mathbf{T}}_j^i$ is the measured relative transformation for a factor between nodes i and j , and Σ_j^i is its associated covariance; $\rho(\cdot)$ denotes a robust kernel (e.g., Huber) to mitigate the influence of outliers; $\log(\cdot)$ is the Lie algebra logarithm mapping from $SE(3)$ to $\mathfrak{se}(3)$; and $\|\mathbf{x}\|_{\Sigma}^2 = \mathbf{x}^T \Sigma^{-1} \mathbf{x}$ denotes the squared Mahalanobis distance. We implement this optimization using the GTSAM library [56], leveraging its efficient sparse linear algebra routines and the Levenberg-Marquardt solver. The resulting optimized poses \mathcal{T}^* accurately integrate the query submap into the reference map, completing the map-merging pipeline.

C. Cross-Device Localization

We extend our framework to collaborative localization with data from heterogeneous devices, often operated by non-expert users. This “*in-the-wild*” data introduces complexities driven by three factors: 1) *motion in diverse patterns* where rapid rotations and head movements induce noise and motion blur;

2) *device heterogeneity*, where diverse camera models and configurations lead to inconsistent Fields of View (FoV) and intrinsics; and 3) *perceptual degradation*, caused by uncontrolled lighting and environmental artifacts. We introduce two mechanisms to address these issues.

MASt3R is trained on undistorted perspective images and achieves ideal performance under these conditions. While our metric localization refines unknown intrinsics to some degree, handling non-perspective or heavily distorted images requires a pre-processing step. For consumer devices (e.g., smartphones, AR glasses), we integrate an undistortion module. This leverages manufacturer-provided SDKs to obtain camera intrinsics and rectify raw images, yielding distortion-free perspective inputs. Furthermore, we extend our approach to handle panoramic imagery from sources such as Google Street View. Panoramic images, typically stored as equirectangular projections, cannot be used directly. We transform them by generating synthetic perspective images via spherical projection. This involves sampling a virtual pinhole view from the panorama, often centered at a zero-degree viewpoint (aligned with the travel direction). As shown in Fig. 5(a), this conversion produces virtual perspective images with a user-defined FoV and virtual intrinsics that are compatible with our pipeline. Additionally, all images are cropped to the same size of reference images, to best utilize the MASt3R model.

Second, crowd-sourced imagery suffers from highly variable quality, including motion blur, occlusions, inconsistent exposure, and sensor noise. To identify perceptually degraded data, we utilize a non-reference IQA method called multi-scale image quality transformer (MUSIQ) [57], which predicts a quality score $\in [0, 100]$ for an image. This IQA score allows us to quantify and filter images with low quality. Fig. 5(b) shows example IQA scores for images captured in day and night conditions, while Fig. 9 visualizes the complete IQA score distribution of our self-collected dataset. We filter out images that do not meet the minimum IQA score threshold.

D. Map Merging with Node Culling and Edge Updating

As submaps are merged, the traversable regions are extended, yet the overall map size inevitably grows linearly. We therefore introduce node culling and edge updating to maintain the expanding map.

1) *Node Culling*: While our map is inherently more compact than dense structure-based alternatives, storing RGB images still incurs significant storage costs. SLAM systems typically manage this growth through keyframe selection heuristics based on spatial overlap [58], parallax [59], or feature tracking stability [19]. However, these purely geometric criteria often neglect perceptual degradation (e.g., motion blur) and temporal difference, which are critical factors in lifelong operation. Outdated nodes can exhibit significant discrepancies arising from environmental changes, thereby degrading the performance of on-demand reconstruction and pose estimation.

To ensure map scalability and long-term robustness, we introduce a probabilistic culling strategy that operates after PGO. Our central idea is to evaluate nodes based on their *Information Contribution* (IC), with the similar idea as [60]. Nodes with

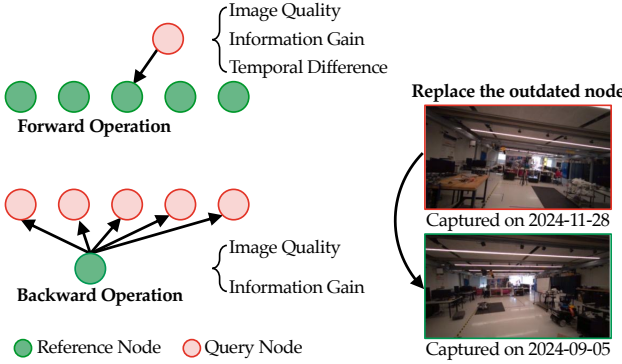


Fig. 6. Illustration of the node culling strategy for lifelong map maintenance. We design the forward and backward operations to remove nodes with little information contribution from the set \mathcal{P}_{CCM} . The retention probability of a node is determined by the joint distribution of its image quality (IQ), information gain (IG), and temporal difference (TD). **(Left)** The arrow direction indicates the comparison logic: the node at the tail is evaluated against the node at the head and will be replaced if redundant. **(Right)** A real-world example showing an outdated reference node (captured on 2024-09-05) being replaced by a more recent node (captured on 2024-11-28).

a low IC, indicating limited utility for future localization or reconstruction, are discarded. The IC is calculated by jointly considering three factors:

- **Image Quality (IQ):** Defined as the IQA score q . Low-quality images (e.g., blur or poor illumination) provide unreliable observations and are prioritized for removal.
- **Temporal Difference (TD):** Represented as the elapsed time $\Delta\tau = \tau_Q - \tau_R$ between the query and reference nodes. This factor penalizes older images, as they may no longer accurately reflect the current environment.
- **Information Gain (IG):** Quantifies the novel geometric information provided by a query node \mathbf{I}_Q relative to an existing reference node \mathbf{I}_R . By reusing results from the MAST3R model, we project the associated pointmap \mathbf{X}_Q^R onto the reference image \mathbf{I}_R . The IG is computed as $g = n/wh$, where n is the number of points projecting outside the bounds of \mathbf{I}_R , and w, h are the image dimensions.

As illustrated in Fig. 6 (left), the culling procedure consists of the forward and backward operations. These are applied exclusively to the set of high-confidence metric-localization pairs, $\mathcal{P}_{CCM} = \{\mathbf{n}_1^R, \dots, \mathbf{n}_{N-1}^R, \mathbf{n}^Q\}$. To minimize computation, we adopt a “generous spawning, conservative culling” strategy, calculating IC only for nodes within \mathcal{P}_{CCM} . Culling is triggered immediately after a new submap merges into the global map. The forward operation processes the new query node, while the backward operation targets existing reference nodes which are connected to any query node. We compute the forward probability for \mathbf{n}^Q as:

$$P_{FW}(\mathbf{n}^Q) = P_{IQ}(q_Q) \cdot P_{IG}(g_Q) \cdot P_{TD}(\tau_R - \tau_Q), \quad (8)$$

while in the backward operation, the probability for each existing reference node \mathbf{n}_i^R is

$$P_{BW}(\mathbf{n}_i^R) = P_{IG}(g_{R_i}) \cdot P_{TD}(\tau_Q - \tau_{R_i}), \quad (9)$$

where $P_{IQ}(\cdot)$ and $P_{IG}(\cdot)$ are sigmoid functions, and $P_{TD}(\cdot)$ is an exponential decay function. Nodes falling below a pre-defined probability threshold are culled. Fig. 6 (right)

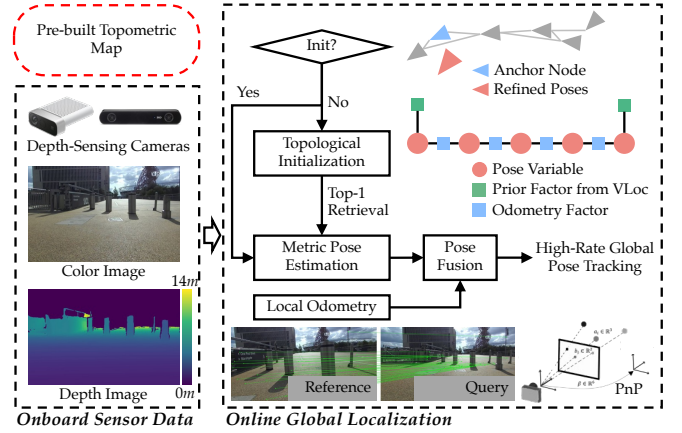


Fig. 7. Pipeline of the localization method using the resulting topometric map. The global and high-rate camera poses are estimated hierarchically through topological initialization, metric pose estimation, and pose fusion. The resulting poses are then used for downstream image-goal navigation.

illustrates a real-world scenario where a node is removed or replaced by a new candidate due to limited IC.

2) *Edge Updating:* We further enhance map connectivity by adding edges in the covisibility and traversability graphs. Initially, the map is constructed from the odometry sequence during the premapping phase, resulting in edges only between consecutive frames. This chain-like structure suffers from topological sparsity. It lacks edges between spatially adjacent but temporally distant nodes (e.g., during loop closures), preventing the graph from representing the true connectivity of the environment. To address this limitation, we augment the CvG by iterating over each node, exploring its spatial neighborhood, and validating covisibility based on the number of matched keypoints between image pairs. Edges meeting the covisibility threshold are dynamically added to the graph. The same augmentation approach is applied to the TrG. While more advanced techniques, such as explicit traversability assessment [24], [61], could further refine the TrG’s edge quality, such methods are beyond the scope of this work.

V. LEVERAGING OPENNAVMAP FOR VISUAL NAVIGATION

We investigate the potential of OPENNAVMAP to serve as the underlying map for autonomous navigation. Adopting the framework from [14], we implement an image-goal VNav system wherein the proposed topometric map facilitates robot navigation to targets specified by goal images.

A. Hierarchical Global Localization

The robot employs a hierarchical localization pipeline to estimate its global pose relative to the map. This approach is specifically applicable to platforms equipped with sensors providing direct depth information, such as RGB-D cameras. This hardware configuration enables a more simple VLoc strategy, in contrast to the collaborative localization approach detailed in Sec. IV-B.

1) *Topological Initialization:* Topological initialization is necessary upon mission start, following a period of pose tracking lost due to insufficient feature correspondences, or after a system restarts. To estimate its initial position inside

the map, the robot executes VPR. This involves comparing a descriptor of the current observation against the complete map to identify the most visually similar candidates. We first retrieve the top-5 candidate nodes using the VPR model. Subsequently, a GV step selects the most confident match to serve as the *anchor node*.

2) *Metric Pose Estimation*: This phase is initiated after successful topological localization and operates at a fixed update rate. In each step, the robot iteratively refines its pose by first retrieving a candidate set of spatially-local nodes from the CvG. The node within this set exhibiting the maximum visual similarity to the current query image is selected as the reference frame. We then establish feature correspondences between the depth-augmented query image and the selected reference image, leveraging the capabilities of MAS3R [3] for robust matching. These 2D matches are converted into 2D-3D correspondences by applying the camera intrinsics and the query’s depth information to back-project the pixels into 3D space. The final camera pose relative to the global frame is then robustly determined using the PnP algorithm [40] combined with RANSAC [41] for outlier rejection.

3) *Pose Fusion*: However, the above metric pose estimation is susceptible to several issues, including domain gaps, viewpoint variations between reference and query images, textureless or visually repetitive scenes, noise in depth measurements, and the latency of the visual processing pipeline. To counteract these effects and enhance pose estimation robustness, we incorporate a pose fusion module. This module integrates the low-frequency VLoc estimates with high-frequency local odometry such as wheel encoders and VIO. The integration yields pose estimates with both improved overall accuracy and a higher update frequency. We formulate pose fusion as a PGO problem, with camera poses serving as the optimization variables. The cost function integrates absolute pose priors from VLoc for global anchoring and relative motion constraints as the odometry factor derived from local odometry. The PGO solver is triggered whenever a new VLoc estimate becomes available. But during the intervals between VLoc updates, poses are propagated solely by the local odometry, which naturally leads to the accumulation of drift over time.

B. Closed-Loop Visual Navigation

Given that the topometric map preserves visual snapshots of the scene, it is inherently well-suited for image-goal navigation tasks. Unlike point-goal navigation, where the target is defined by coordinates, image-goal navigation directs the robot to a target specified by a reference image, significantly enhancing the human-robot interaction. It also allows for flexible inputs, such as images from Internet. Furthermore, the system is extensible; image goals can be transformed into other formats, and the topological nodes can be augmented with visual-language embeddings to support semantic goals (e.g., “go to the kitchen”). Once the robot receives a goal image, we first identify its corresponding topological node using the same initialization pipeline described previously.

Planning utilizes a hierarchical structure encompassing both global path and local motion planning. For the global path

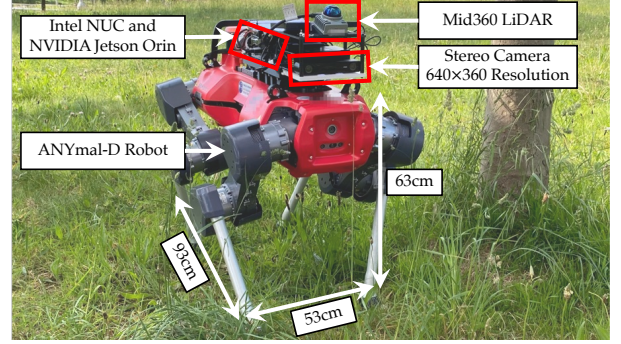


Fig. 8. The VNav system is deployed on a real-world ANYmal-D robot, equipped with onboard stereo cameras and computing units.

planning, we use Dijkstra’s algorithm to find the shortest path $P = \{\mathbf{n}_S, \dots, \mathbf{n}_i, \dots, \mathbf{n}_G\}$ within the TrG. The path cost is determined by the traversability value between nodes. For the local motion planning, once the robot reaches the current subgoal \mathbf{n}_i , the next subgoal \mathbf{n}_{i+1} is projected into the robot’s body frame. Using this projected goal, the local planner generates a collision-free path and executes the required control commands to drive the robot toward the next subgoal.

VI. EXPERIMENTAL SETUP

This section details the experimental setup used to evaluate the proposed system, covering implementation specifics, datasets, and evaluation metrics.

A. Implementation Details

The proposed collaborative mapping and localization system is implemented in Python. Importantly, all learning-based models were utilized without additional fine-tuning. Several implementation details are elaborated as follows.

1) *Submap Construction*: We further explain details in Sec. IV-A2. Submap is constructed from the collection of visual data and corresponding odometry estimates at a fixed rate. To manage data density, we select keyframes when the displacement from the previous keyframe surpasses a translational threshold of $3.9m$ or a rotational threshold of 60° . These selected keyframes are used to initialize the submap. The different layers of the submap, the OdG, TrG, and CvG, are simply built by directly linking consecutive keyframes. For the TrG, the above operations assume that the local connectivity between sequential keyframes is traversable. This initial submap is subsequently transferred to the central server for subsequent map merging.

2) *Visual Place Recognition Models*: A unified VPR model is employed for the collaborative localization and the global localization during navigation. We employ the pre-trained CosPlace [23] model to extract the place descriptor for each image. The ResNet-18 version of CosPlace was chosen for its lightweight architecture and competitive performance. This model has $11M$ parameters and provides a concise 256-D descriptor. While more powerful VPR models exist (e.g., EigenPlaces [62], AnyLoc [63], and MegaLoc [64]), our system’s architecture is fully compatible with these alternatives, allowing for performance scaling if higher recall is required.

We also include a comparative analysis of the system's performance using several VPR models to demonstrate the compatibility of our system, as shown in Sec. VII-A.

3) *Visual Navigation*: The VNav system is developed based on the established navigation stack from [65], into which we integrate our proposed collaborative localization and mapping approach. The system's performance is validated across simulated and real-world environments.

Our simulation employs a two-wheeled differential-drive robot operating within the high-fidelity Matterport3D environment [66], which provides the photo-realistic 10Hz visual and depth inputs essential for evaluation. We selected three environments for testing, covering both home and office settings². Local odometry is obtained by applying the ICP algorithm directly to point clouds generated from depth images. Vision-based pose estimation (1Hz) is fused with local odometry to produce the final pose at the odometry's frequency. Local motion planning is handled by iPlanner [67], a learning-based planner that takes one depth image as input. Simulated experiments were conducted on a desktop PC equipped with an Intel i9 processor and an NVIDIA GeForce RTX 4090 GPU.

Real-world experiments were conducted in both indoor and outdoor environments. We deployed our system on the ANYmal-D quadruped robot (Fig. 8). The robot's local odometry is sourced from a 20Hz proprioceptive state estimator [68] that fuses data from an IMU, joint encoders, and contact sensors. The robot is equipped with a front-facing ZED2 stereo camera (640×360 resolution) that provides RGB images and depth maps; the latter are generated by its internal stereo matching algorithm with a range of up to $15m$. For local motion planning, we employed the model-based Falco method [65], which requires a local 3D map as input. In our implementation, this map is generated on-the-fly from a single-frame point cloud. Computational tasks are distributed across two onboard computers: an Intel NUC manages local planning and visualization, while an NVIDIA Jetson Orin is dedicated to executing the global planner and the VLoc algorithm.

B. Datasets for Collaborative Localization

1) *Self-Collected Datasets*: We use the Meta Project Aria glasses [17], which are equipped with two wide-angle grayscale cameras, a front-facing RGB camera, a consumer-grade IMU, and GPS to collect data in real-world environments. The data spans two countries over a period of 3.5 months, comprising 35 sequences and totaling over 18.7km of trajectories. Sequences are organized into three geographic regions (R0-R2). R0 consists of data from a compact vineyard acquired during a single session; R1 contains recordings from a mid-sized campus capturing both day and night conditions; and R2 spans a large-scale area featuring buildings, parks, roads, and shopping centers, recorded from summer to winter. Five users with varied behavior patterns contributed to the data collection, introducing challenges such as wide viewpoint

²We selected three environments³, corresponding to Env0-2 in Table VI. The scene IDs, ordered by increasing size, are 17DRP5sb8fy, EDJbREhghzL, and B6ByNegPMK.



Fig. 9. Overview of our self-collected dataset and trajectories captured by various devices. The data collected using Aria glasses covers diverse environments, including offices, campuses, shopping centers, and vineyards, across two countries, spanning approximately 3.5 months, 35 sequences, and over 18.7km of traversed distance.

variations (e.g., forward and backward facing), appearance changes, and irregular motion trajectories.

Ground truth (GT) poses were generated using Meta's cloud-based SLAM service [17], providing outputs in the global coordinate frame. Recent research have qualitatively validated the high accuracy of such poses [69] at city scale. All images are post-processed to anonymize identifiable information, such as by blurring faces. A summary of the datasets is provided in Fig. 9. These sequences follow the map-free benchmark [2] structure data and are processed into formats for evaluation of two collaborative localization stages:

- **Topological Localization**: We manually selected 4 reference sequences from R2. For each of these references, we then selected corresponding query sequences also from R2 that have spatial and visual overlap, resulting in a total of 26 query sequences.
- **Metric Localization**: We randomly select 57 query images per scene from R2. For each query image, we select the corresponding reference images based on proximity (within $5m$) and verified visual overlap (measured by the number of matched keypoints). Query images are captured from varying perspectives and times of day, making relative localization highly challenging. GT relative transformations are provided.

We also process the dataset for the complete **Map Merging** experiments. We use all sequences from R0-R2. Each sequence is split into segments of at most $300m$, with keyframes selected using a distance-based threshold⁴. This setup simulates short-term data capture from multiple users, resulting in 68 segments. We provide camera intrinsics and extrinsics, timestamps, local VIO poses, and GT poses.

2) *Public Datasets*: Metric localization (Section VII-B) is additionally evaluated with two public datasets: Map-Free

⁴Translation and rotation thresholds are $3.9m$ and 60° , respectively.

(65 validation scenes) [2] and GZ-Campus (30 scenes) [14]. To evaluate map merging performance with heterogeneous devices, we expand our datasets with additional data sources. R1 is augmented with three sequences from an iPhone 16 Pro (using the kit from [70]) and one sequence from a vehicle-mounted camera [48]. R2 is enriched with Google Street View panoramas spanning 2012-2024. Additionally, we employ the 360Loc dataset for quantitative map merging experiments, by leveraging its GT poses. Leveraging its captured panoramic images, we simulate cross-device queries by projecting such images into perspective views with varying intrinsics and extrinsics. Details, including data processing and illustrative examples, are provided in the **Supplementary Material**. [71].

C. Evaluation Metrics

We evaluate the system, in terms of collaborative localization and VNav, with different metrics.

1) *Collaborative Localization*: For topological localization, the objective is to determine whether a query node corresponds to a reference node at the same place. We use retrieval metrics, defining a correct match as one within a tolerance of $[7.5m, 75^\circ]$. This threshold is chosen to reflect practical navigation requirements.

- **Recall@1** measures the system’s ability to find valid places. It answers: “Of all the query nodes that should have had a correct match in the reference map, what percentage did the system successfully find and rank as its top-1 result?” It is a common metric for VPR.
- **Precision@1** measures the reliability of the system’s single best guess. It answers the question: “Of all the query nodes where the system claimed to find a top-1 match, what percentage of those matches were actually correct?” Since queries may lack a true match, the ability to reject these false positives is crucial for system stability.
- **Average@1**: The average of Recall@1 and Precision@1.

For metric localization, the goal is to estimate the precise relative pose. We follow [2] to report these metrics:

- **Precision@[1m, 10°]** is defined as the percentage of pose error of queries within a threshold. This metric evaluates the system’s ability to produce accurate estimates.
- **AUC (Area Under the Curve)@[1m, 10°]** measures the quality of system confidence estimation. It answers: “How effectively can the system’s confidence score separate correct matches from incorrect ones?”

For map merging, it is a process that couples topological localization, metric localization, PGO, and node culling. We primarily evaluate it in terms of the global pose accuracy of the final map. Our metric is the ATE [72] in terms of RMSE. ATE measures the overall drift and alignment of the entire estimated pose against the GT pose. We also provide qualitative results for map merging that incorporate heterogeneous devices.

2) *Visual Navigation*: In the simulated environment, the performance of our VNav system is quantified using two standard metrics: the total time required to reach the goal and the actual path length executed by the robot. These metrics also highlight the inherent trade-offs and performance limitations between our fully vision-based VNav system and traditional

approaches that benefit from perfect knowledge, such as GT poses and detailed local maps, for planning and execution.

VII. EXPERIMENTAL RESULTS

Our experimental evaluation is organized into four main parts. First, we validate the proposed collaborative localization pipeline, assessing performance on the critical subtasks of topological and metric localization in Sec. VII-A and VII-B. Second, we evaluate the system’s map merging capabilities, specifically examining performance with and without heterogeneous devices in Sec. VII-C and VII-D, respectively. Third, we demonstrate the VNav system’s performance in both simulated and real-world environments in Sec. VII-E. Finally, we conduct an ablation study to investigate the necessity of node culling for lifelong operation in Sec. VII-F.

A. Experiments on Topological Localization

1) *Settings and Baselines*: To evaluate our proposed sequence matching and GV modules, we conduct experiments on our self-collected dataset. We use MASt3R [3] as the 2D feature matcher for the GV stage. Our method is compared against SeqSLAM [34] (using a sequence length of 20). We also compare four SoTA VPR models: **AnyLoc** [63], **NetVLAD** [73], **CosPlace** [23], and **EigenPlaces** [62]. The global descriptor dimensions for these models are 49152, 4096, 256, and 256, respectively.

2) *Results Analysis*: Table I reports the results of topological localization, where N_{Pos} denotes the number of query with positive loops, while N_{Query} represents the total number of query images. A lower ratio implies that a larger fraction of queries do not have any positive loops. We observe that CosPlace offers the optimal trade-off between accuracy and efficiency, matching AnyLoc and surpassing NetVLAD with a compact (256-D) descriptor. This is mainly attributed to the classification-based training objective that scales CosPlace to massive datasets to capture diversity and the large margin cosine loss to enforce this model to extract discriminative and lightweight embeddings.

Additionally, post-processing VPR’s output with sequence matching and GV yields a precision gain of at least 10 points. Our results show that classical SeqSLAM’s reliance on fixed sequence lengths reduces adaptability. In contrast, our DP-based approach performs a wider search on the difference matrix, resulting in higher recall, particularly on Reference 0. GV also serves as a mandatory filter for inconsistent candidates. It provides the most significant precision boost in difficult scenarios (Reference IDs 1 and 2) where raw VPR retrieval is noisy. By filtering these outliers, we reduce the computational load for metric localization, albeit at the cost of occasionally removing valid loop closures.

B. Experiments on Metric Localization

1) *Settings and Baselines*: Metric localization entails estimating the 6-DoF relative pose of a query image with respect to a set of reference images. We conduct evaluations across three diverse datasets that pose distinct challenges:

TABLE I

RESULTS OF TOPOLOGICAL LOCALIZATION ON OUR SELF-COLLECTED DATASET (R2) WITH METRICS: PRECISION@1 [%] AND RECALL@1 [%] WITHIN A THRESHOLD OF [7.5M, 75°]. THE FIRST AND SECOND BEST RESULTS ARE HIGHLIGHTED IN RED AND BLUE, RESPECTIVELY.

Ref.	Sequence ID	0	1	2	3	
	$N_{Pos} : N_{Query}$	838 : 999	208 : 479	235 : 547	187 : 215	
VPR	Matching	GV	Prec. Rec. Avg.	Prec. Rec. Avg.	Prec. Rec. Avg.	
NetVLAD [33]	SingMatch	✗	76 61 68	18 28 23	16 26 21	67 31 49
	SingMatch	✓	97 59 78	79 26 53	85 26 55	98 30 64
	SeqSLAM	✗	75 56 66	21 36 29	21 36 29	78 55 67
	SeqSLAM	✓	97 54 76	93 32 62	88 35 62	99 51 75
	DP (Ours)	✗	81 80 80	32 63 48	21 35 28	82 69 75
	DP (Ours)	✓	98 77 88	88 58 73	84 32 58	98 66 82
CosPlace [23]	SingMatch	✗	77 64 71	19 30 24	20 34 27	69 35 52
	SingMatch	✓	96 63 80	75 30 52	92 34 63	99 34 66
	SeqSLAM	✗	76 60 68	20 33 26	20 33 27	79 58 69
	SeqSLAM	✓	96 58 77	82 30 56	88 32 60	100 56 78
	DP (Ours)	✗	80 77 79	24 41 32	28 51 40	80 64 72
	DP (Ours)	✓	97 75 86	78 40 59	92 48 70	97 62 79
EigenPlaces [62]	SingMatch	✗	77 63 70	19 30 25	20 34 27	72 41 57
	SingMatch	✓	96 61 79	73 30 51	85 33 59	96 40 68
	SeqSLAM	✗	76 61 68	23 39 31	21 35 28	79 57 68
	SeqSLAM	✓	96 58 77	83 38 60	83 34 58	97 55 76
	DP (Ours)	✗	81 80 80	24 41 32	25 44 35	77 52 65
	DP (Ours)	✓	98 77 87	73 38 56	82 40 61	98 50 74
AnyLoc [63]	SingMatch	✗	80 79 80	31 60 46	32 63 48	83 74 78
	SingMatch	✓	95 77 86	75 57 66	81 63 72	93 66 80
	SeqSLAM	✗	77 65 71	32 60 46	32 63 48	82 71 77
	SeqSLAM	✓	96 62 79	80 53 67	83 60 72	98 65 81
	DP (Ours)	✗	82 86 84	31 59 45	36 74 55	86 92 89
	DP (Ours)	✓	96 82 89	74 54 64	80 68 74	94 85 89

- Map-Free** [2]: Represents tourist-centric scenarios characterized by object-focused imagery, long-term temporal changes, and extreme viewpoint variations ($> 90^\circ$).
- GZ-Campus** [14] and **Self-Collected**: Capture daily routine routes in large-scale environments, introducing challenges such as structural ambiguities, repetitive textures, and large spatial baselines.

To fairly evaluate robustness to view sparsity, we randomly sample 10 groups of N reference images per scene and report results averaged over all M scenes. This reduces bias from reference view selection and ensures statistically robust accuracy and AUC measurements. And several SoTA methods are compared as baselines:

- Structure-based Methods**: We evaluate **HLoc** pipelines configured with different keypoint extractors: **HLoc (DISK+LG)** [74] and **HLoc (SuperPoint+LG)** [75], both utilizing LightGlue [76] for matching. These methods rely on COLMAP [8] to construct an explicit SfM map and then localize a query image within the map [55].
- VPR-based Topological Methods**: We employ **VPR (CosPlace-256)** and **VPR (NetVLAD-4096)**. They approximate metric localization by assigning the pose of the top-1 retrieved reference image to the query.
- Pose Regression Methods**: We include **Reloc3R** [77], which regresses relative pose between reference images and the query image via a neural network, followed by motion averaging for the final estimate.
- 3D GFM-based Methods**: We compare against **DUST3R** [4] and **MASt3R** [3] utilizing global optimization. Our method, denoted as **Ours (DUST3R)** and **Ours**

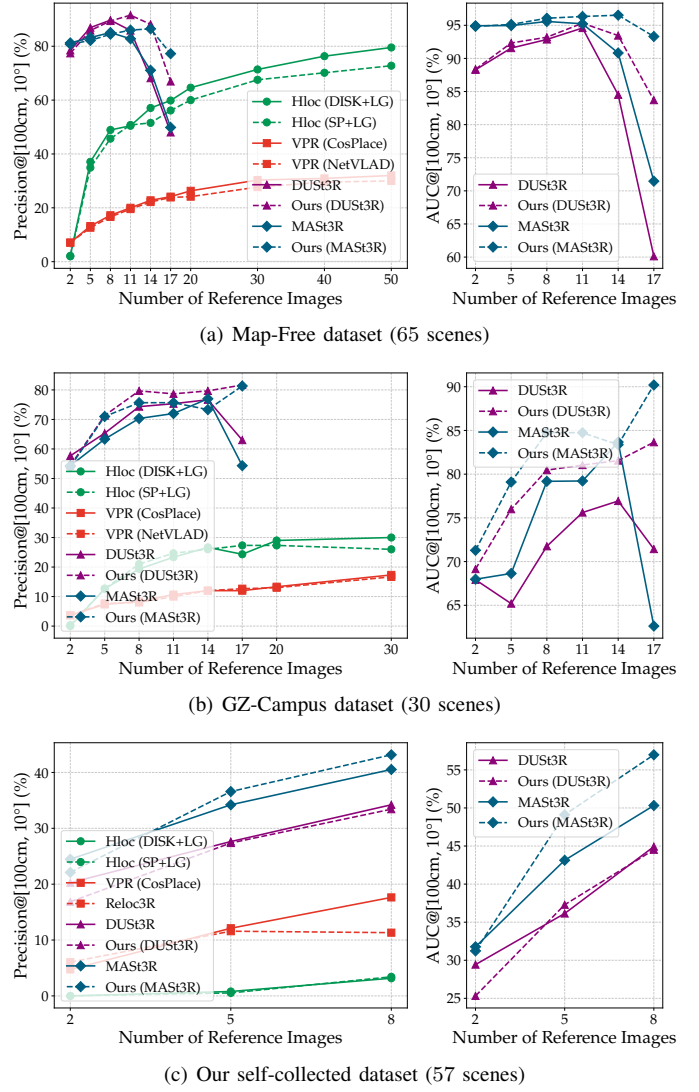


Fig. 10. Evaluation of metric localization performance across three datasets. We report Precision [100cm, 10°] (%) and Area Under the Curve (AUC) as a function of the number of reference images N . The range of N varies across datasets, this is because the maximum number of all available views in each scene is different. To ensure statistical robustness, the performance for each N is averaged over 10 randomized selections of reference groups across all scenes in the dataset. Note that AUC curves are plotted exclusively for DUST3R- and MASt3R-based methods (including ours), as other methods do not output explicit estimation confidence scores.

(MASt3R), distinguishes itself by introducing a confidence map calibration mechanism to refine the optimization. Unlike the first category, these latter three categories (VPR, Regression, and GFM) operate without storing explicit 3D environment geometry.

2) **Results Analysis**: Fig. 10 reports the pose estimation accuracy across three datasets. We specifically plot the AUC for DUST3R- and MASt3R-related methods since they output estimation confidence. On the Map-Free dataset, our method attains over 80% precision using only two reference images per query, fully demonstrating the potential of 3D GFMs. In contrast, HLoc (DISK+LG) requires more than 50 reference images to achieve comparable precision. Furthermore, its performance degrades rapidly when fewer than five views are available, a failure is attributed to insufficient triangulation.

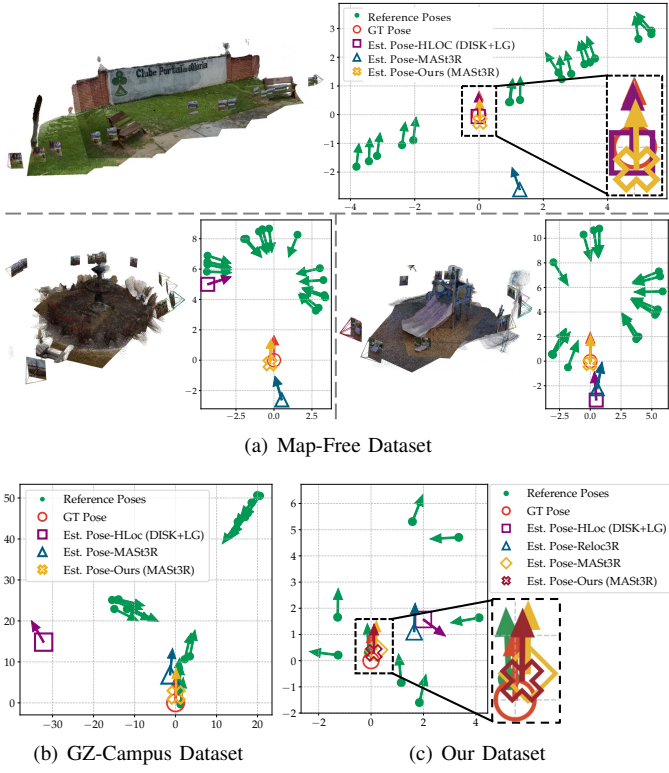


Fig. 11. Sample results of metric localization on three datasets. The accompanying local reconstructions are generated as by-products using both reference images (provided GT poses) and query images. The pose distributions of reference images vary from different datasets.

The remaining two datasets present greater challenges for all methods. As shown in Fig. 11, reference poses in the GZ-Campus dataset are distributed irregularly, with some lying further than 50m from the query. Even under these conditions, our method consistently outperforms HLoc-based approaches, maintaining higher precision and demonstrating a greater benefit from additional views (*i.e.*, 5-11 views). Also, other baselines using structure-free maps still fail to achieve comparable accuracy on these challenging datasets.

We further analyze the utility of confidence map calibration, which serves to enhance optimization and quantify the reliability of the final estimates. Our method consistently achieves higher precision and AUC than DUS3R and MAS3R in most scenarios. Notably, when the number of views (≥ 14) increases in the Map-Free and GZ-Campus datasets, all 3D GFM-based methods exhibit a performance decline. This drop likely stems from an increased parameter for optimization and higher outlier rates in pointmap prediction [78], or insufficient optimization convergence, exposing limitations in DUS3R-series methods. However, our calibration step mitigates this degradation more effectively than the baselines. Furthermore, the AUC analysis confirms that the CCM serves as a superior indicator of reliability compared to uncalibrated confidence, making it highly effective for rejecting false matches.

3) *Map Size Analysis*: We evaluate the theoretical map size of our solution to demonstrate its lightweight nature, following the estimation approach in [26]. Our method stores only resized RGB images, whereas HLoc-based methods must store a 3D point cloud, feature descriptors, covisibility information,

TABLE II
THEORETICAL MAP SIZE PER IMAGE AND RELATIVE RATIO OF BASELINES COMPARED TO OURS.

Methods	Parameters	Map Size [MB]
Ours	$H = 512, W = 288, C \in (0, 1]$	$0.423CN$
HLoc (DISK+LG)	$M = 5000, D = 128$	$1.22N (\frac{2.89}{C} \times)$
HLoc (SP+LG)	$M = 4096, D = 256$	$2N (\frac{4.66}{C} \times)$

* N : Number of reference images for a map.

TABLE III
THEORETICAL AND EMPIRICAL MAP SIZES FOR DIFFERENT EXAMPLES.

Dataset Scene	Method	Theoretical Size [MB]	Empirical Size [MB]
Map-Free s00524, $N = 17$	Ours	$7.2C$	$1.3 (C \approx 0.18)$
	HLoc (DISK+LG)	20.7	22.4
	HLoc (SP+LG)	34.0	12.3
GZ-Campus s00039, $N = 30$	Ours	$12.7C$	$1.8 (C \approx 0.14)$
	HLoc (DISK+LG)	36.6	39.7
	HLoc (SP+LG)	60.0	21.1
Self-Collected G2-R4, $N = 4273$	Ours	$1802.7C$	213.0 ($C \approx 0.12$)

and a visual dictionary.

We simplify the estimate by considering only the feature descriptors, which constitute the largest portion of the map. With N reference images, M maximum number of extracted features per image, and D -dimensional descriptors at half-precision (2 bytes/dim), the map size is $N \times 2DM$ bytes. For methods using structure-free maps, the stored JPEG images constitute the vast majority of the map’s data. The map size is $N \times (3WHC)$ bytes, where W and H are image dimensions and C is the average JPEG compression ratio. Table II reports the theoretical storage sizes for our method and HLoc-based approaches. We also compare theoretical and empirical map sizes for three selected scenes in Table III. Our method consistently achieves a much lower storage requirement. Note that HLoc’s empirical size is lower than theoretical estimates due to sparse feature extraction in texture-less scenes, though this comes at the cost of localization precision. Finally, while 3D GFMs introduce a fixed overhead for model weights (*e.g.*, 2.6GB for MAS3R), this cost is independent of scale, making our solution increasingly efficient as the map grows.

C. Experiments on Map Merging with Homogeneous Devices

Map merging incrementally aligns multiple submaps into a common coordinate frame, integrating our topological localization, metric localization, PGO, and node culling strategies. The “InOrder” baseline processes sequences chronologically. This scenario is inherently less challenging, as consecutive submaps were captured with sharing spatial overlap, facilitating initialization. In contrast, to simulate crowd-sourced data, where temporal proximity does not guarantee spatial overlap, we evaluate the system using randomly shuffled input sequences. We denote these trials as $Ri-j$, representing the j -th random experiment performed on data from Region i .

Table IV reports the ATE against ground truth. We observe that ATE values fluctuate across different random orders, as the input sequence alters the factor graph topology and the

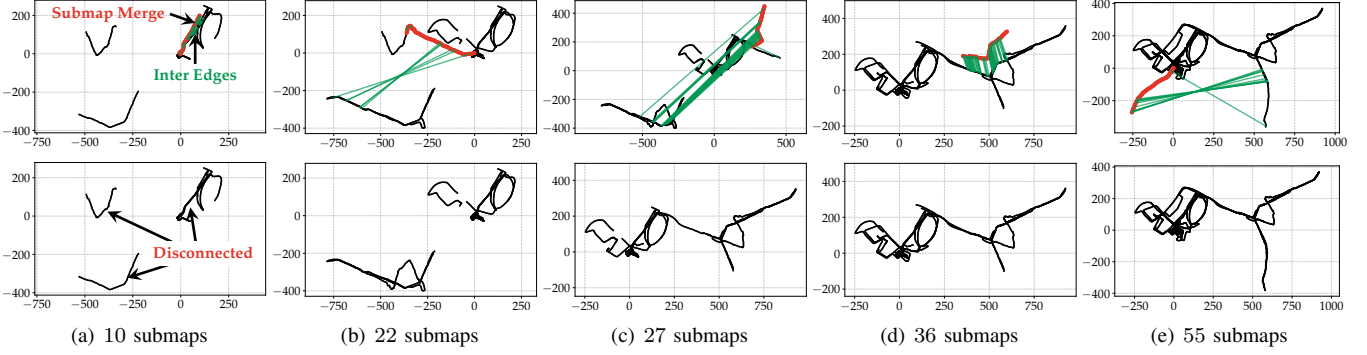


Fig. 12. Incremental map merging with submaps added in random order. Disconnected submaps, as in (a), do not affect pose graph optimization. Example shown uses data from R2-4 (top: before merging, bottom: after merging). Green lines indicate reliable loop closures to establish inter-submap edges.

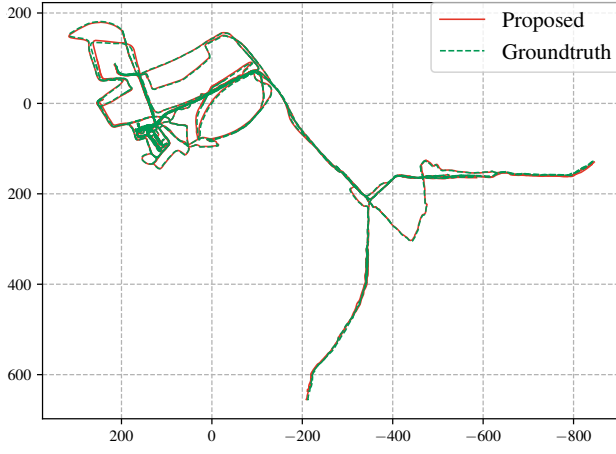


Fig. 13. Estimated trajectory of R2-4 from our multi-session mapping system and GT trajectory from Aria glass-provided SLAM service.

TABLE IV

ABSOLUTE TRAJECTORY ERROR (ATE) ACROSS DIFFERENT SCENARIOS IN OUR SELF-COLLECTED DATASET.

Data	Distance Time Spans	Shuffle	Translational ATE [m]	Rotational ATE [deg]
R0-InOrder				
R0-0	0.6km	N	0.47	0.70
R0-1	6mins	Y	0.65	0.86
R1-InOrder				
R1-0	2.5km	N	1.18	0.44
R1-1	18hours	Y	2.39	1.15
R2-InOrder				
R2-0		Y	1.51	1.71
R2-1		Y	2.30	1.10
R2-2		Y	2.87	1.52
R2-3	15.7km	Y	2.30	1.56
R2-4	110days	Y	1.93	2.06
R2-5		Y	1.78	0.98
R2-6		Y	2.05	1.52
R2-7		Y	1.80	1.35
R2-8		Y	1.72	0.79
			2.58	1.00

*Distance and time spans are the properties of the entire dataset

subsequent optimization trajectory. This random ordering is particularly challenging for Region R2, where loop closures between the global map and incoming submaps may be initially absent due to temporal disconnects. Fig. 12 illustrates the incremental map merging process for trial R2-4. Here, our method successfully establishes inter-submap constraints

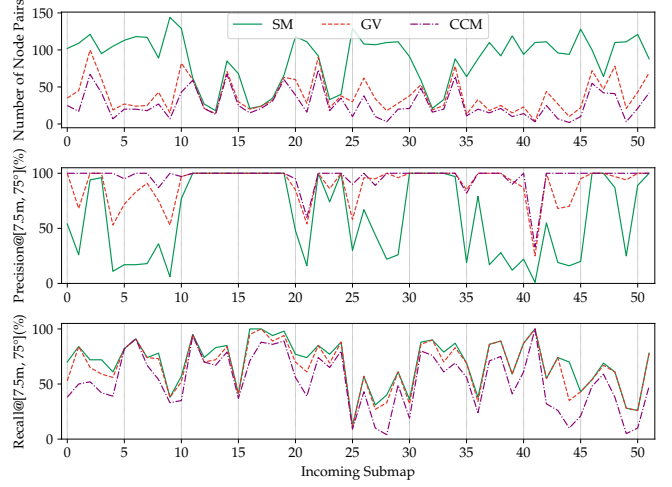


Fig. 14. Evolution of candidate match statistics on the R2-InOrder sequence. The plots display the count of candidate node pairs (corresponding \mathcal{P}_{SM} , \mathcal{P}_{GV} , and \mathcal{P}_{CCM}), precision, and recall across incoming submaps. We compare the initial sequence matching against subsequent filtering stages: geometric verification (GV) and calibrated confidence map (CCM). Observation: Both GV and CCM serve as effective filters; they significantly enhance precision by rejecting false positives, with only a marginal reduction in recall.

and performs PGO, while robustly handling the presence of initially disconnected submaps. Based on these results, we highlight two key findings. First, although random ordering heightens the risk of false positives, our system maintains consistent performance. This is primarily attributed to the GV and CCM modules (using fixed thresholds across all trials). The system thus maintains high global accuracy (max translational and rotational ATE are $< 3.0m$ and $< 2.1^\circ$ respectively over 15.7km). Second, occasionally, submaps may remain isolated due to a lack of valid loop closures. Our system is designed to handle this by maintaining these components as separate until valid and reliable constraints are detected, at which point they are merged into the global map (Figs. 12(b)–12(c)).

Fig. 14 shows how GV and CCM reduce false positives in candidate node pairs during R2-InOrder map merging, reporting candidate count, precision, and recall. While GV verifies local feature matches, CCM acts as a stricter filter by assessing metric localization quality. Although these two filters occasionally reduce recall by rejecting valid connections with poor pose estimates, it is essential to prevent wrong or

TABLE V

ABSOLUTE TRAJECTORY ERROR (ATE) MEASUREMENTS ACROSS DIFFERENT SCENARIOS IN THE 360LOC DATASET.

Scene	Spatial Extent [m]	Session Number	Translational ATE [m]	Rotational ATE [deg]
Atrium	65 × 36	5	0.548	0.809
Concourse	93 × 15	4	0.498	0.904
Hall	105 × 52	5	1.107	2.998
Piatrium	98 × 70	4	1.113	0.989

unreliable edges from degrading the subsequent PGO.

D. Experiments on Map Merging with Heterogeneous Devices

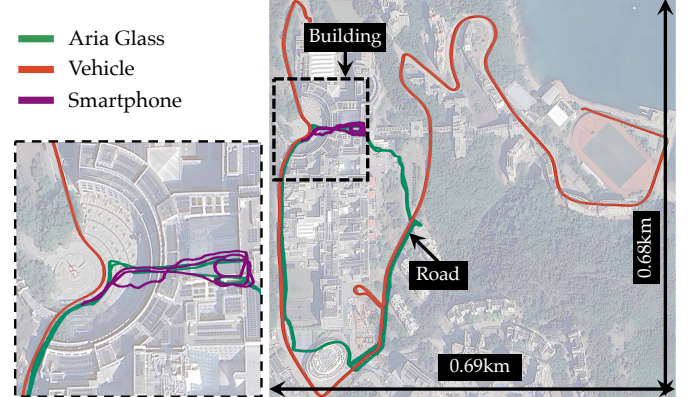
We further evaluate our framework’s extensibility by integrating data from heterogeneous devices. This experiment is divided into two parts. The first part is the experiment using the modified 360Loc dataset, where each sequence is post-processed to simulate the cross-device data collection, *i.e.*, varying camera intrinsics, by providing both the quantitative and qualitative results. The data were collected in a campus environment over a one-week period. The second part is the experiment using our self-collected dataset, where we use the Aria Glass data as the base map, and progressively merge new submaps from three different sources: a pedestrian-carried iPhone, a vehicle-mounted camera, and Google Street View.

1) *Results on 360Loc Dataset:* Map merging performance with the ATE against GT is shown in Table V. Within each scene, the camera models in each session are different, which is good for evaluate for cross-device localization and mapping. Performance drops in the outdoor sequences (Hall, Piatrium) compared to the indoor ones (Atrium, Concourse), suggesting that the collaborative localization pipeline is more effective in indoor environments. Due to the limited space, we show the merged map in the supplementary material [71].

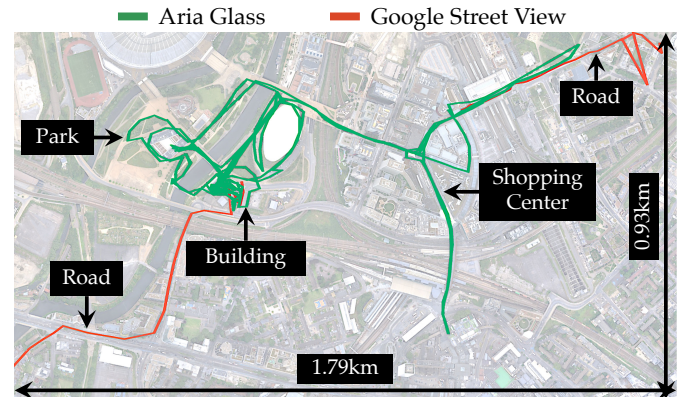
2) *Results on Self-Collected Dataset:* Fig. 15 illustrates the resulting global maps for R1 and R2, overlaid on satellite imagery using GPS data. Based on above experiments, we observe that data collection using only homogeneous devices presents several limitations. Specialized devices (*e.g.*, Aria Glass) capture rich, multi-sensor data but have restricted access. Conversely, smartphones and public street-view platforms enable broad participation and flexible updates. Vehicle-mounted cameras offer large-scale collection but are limited to vehicle-accessible environments. By fusing these heterogeneous sources, our framework constructs a more comprehensive and extensible map, overcoming these individual limitations. As shown in Fig. 16, the expanding map progressively extends image-goal path planning capabilities to new environments. These results highlight the practical utility of our framework for lifelong updates.

E. Experiments: Image-Goal Visual Navigation

We evaluate our VNav system by the image-goal navigation task, where the target is defined by a goal image and the robot is commanded to autonomously navigate to the goal image.



(a) Mapping R1 with 13 sessions: 8 (Aria) + 2 (Vehicle) + 3 (Phone)



(b) Mapping R2 with 57 sessions: 55 (Aria) + 2 (Google Street View)

Fig. 15. Experiments on multi-session mapping with heterogeneous devices across two regions. The estimated map is rigidly transformed into the East-North-Up coordinate system and aligned onto the Google satellite image, enabled by the availability of GPS data for outdoor sequences.

1) *Simulated Visual Navigation Experiments:* We evaluate the VNav system in both simulated and real-world environments. In the simulated setting, the robot is sequentially assigned a series of image goals to reach. Table VI compares VNav against a SoTA LiDAR-based navigation system [65] (using GT localization and Falco for planning). Fig. 17 visualizes the VNav route on the Env1, with the associated topometric map representation and navigation path. Due to the limited FoV of the camera, VNav occasionally encounters local minima, requiring frequent rotation. While this increases the time to reach the goal, it does not significantly affect the total path length, demonstrating that VLoc maintains robust and accurate localization throughout the task. And the map-free path planning is still feasible for collision avoidance.

2) *Real-World Global Path Planning Experiments:* Fig. 16 demonstrates metric-level global planning from a fixed origin to a goal image. This validates the lifelong scalability of our framework, where integrating new submaps continuously extends the planning horizon. Fig. 16(e) shows that the system enables localization and navigation using an image from a phone. By encoding metric coordinates, the system eliminates scale ambiguity and enables shortest-path planning, allowing newly added routes to optimize the overall trajectory. However, maintaining global consistency is critical to this process. To illustrate this, consider a scenario with two submaps connect-

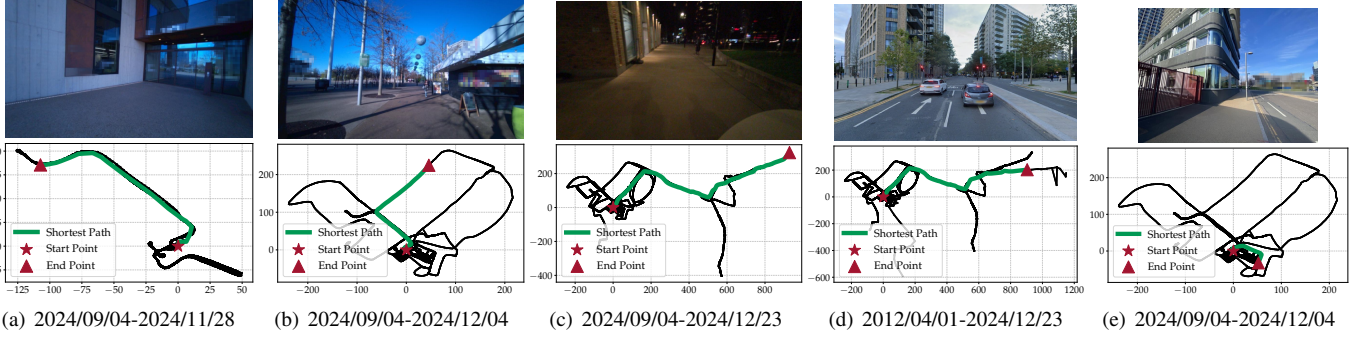


Fig. 16. Global path planning on the topometric map at different mapping stages (a)–(e). The caption for each subfigure indicates the time span of the accumulated map data. As the map expands with new submaps, shortest-path navigation becomes feasible to an increasing number of destinations. Goal Image Sources: (a)–(c) Aria glasses (frames selected from the raw data collection stream of the last submap), (d) Google Street View, and (e) a smartphone. Note that all paths originate from the same fixed starting point on the map.

TABLE VI
NAVIGATION PERFORMANCE IN SIMULATED ENVIRONMENTS.

		Navigation Time [s] and Path Length [m]		
Localization	Planning	Env0 [home]	Env1 [home]	Env2 [office]
GT	Falco	40.3s/25.5m	42.7s/28.3m	266.9s/220.7m
Ours	iPlanner	50.0s/28.6m	52.9s/29.1m	280.3s/223.7m

ing the same start and end points. Submap 1 has an actual length of 10m but is erroneously estimated as 9m, whereas submap 2 has an actual length of 9m but is estimated as 10m. Without metric consistency, the planner would incorrectly select submap 1 due to its shorter estimated cost, despite submap 2 being physically shorter. By enforcing consistency across all integrated submaps, our system avoids such sub-optimality. This above feature allows the map coverage to expand continuously over time while guaranteeing the precise navigation to distant goals.

3) *Real-World Visual Navigation Experiments*: We evaluate the complete VNav system, comprising VLoc against our proposed topometric map, global path planning, and local motion planning, in three real-world environments. These experiments are denoted as **Lab** is a hybrid indoor-outdoor laboratory setting; **Bridge** is an outdoor route between two buildings, including a bridge crossing; and **Building** is a building perimeter traversal with numerous turns. Since the current VNav system only allows the robot to navigate inside the map, we manually move the robot at two arbitrary positions and start the autonomous navigation. But the starting position to the robot, is unknown. The next-goal image is sent to the robot sequentially after the robot reaches the current goal.

In Lab, the robot sequentially executed three image-goal navigation tasks. As shown in Fig.18, the system effectively tracked the robot’s pose despite varying outdoor lighting. The local perception and planning modules enabled obstacle avoidance; however, the absence of a local map occasionally caused zig-zag motions when encountering persistent obstacles such as walls. We repeated the experiment four additional times at different time slots. As shown in Fig. 18(a), the robot successfully navigated from an indoor lab to an outdoor path, autonomously passing through narrow doorways.

Trajectories for the same route, estimated by our VLoc

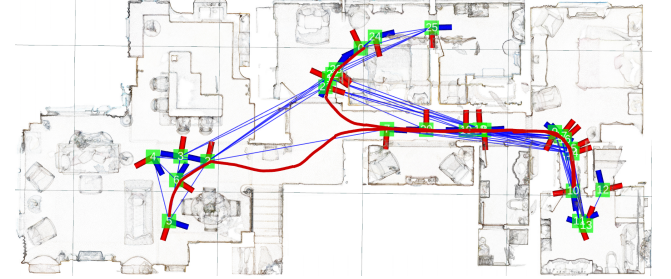


Fig. 17. The VNav system is evaluated in a simulated home environment (Env1), where the robot is tasked with sequentially navigating to a series of image goals. The traversed path is visualized as a red trajectory, while the underlying topometric map is represented as a graph structure: nodes (green) are connected by traversability edges (blue).

module, remained consistent even with significant illumination changes at night. The 160m route was completed in approximately 312s (average speed of 0.5m/s), demonstrating robustness to varying sensor noise from indoor/outdoor lighting.

In Bridge and Building (Fig. 19), we further tested the system’s capabilities. Bridge required the robot to traverse a bridge with sparse visual features.

Here, the MASt3R model was critical for reliable feature matching and relative pose estimation against the global map. This low-rate pose estimate is fused with high-rate local odometry to generate a high-frequency pose output, ensuring accurate navigation to the goal. Building involved complex turns requiring accurate localization for timely maneuvering; relying on odometry alone would accumulate drift and lead to incorrect decisions. The supplemented video offers a detailed visualization of the robot’s behavior in Lab and Building.

F. Experiments: Node Culling for Lifelong Operation

While node culling reduces map storage and discards outdated nodes, it risks erroneously removing necessary information. This section investigates the impact of the culling strategy on map merging and VLoc for the downstream VNav task.

1) *Impact on Map Merging*: To validate our node culling strategy for lifelong operation, we conducted map merging experiments on Lab sequences spanning three months. These sequences are manually selected from R2 as their features in high spatial overlap alongside significant lighting and viewpoint variations. We evaluated performance based on the final

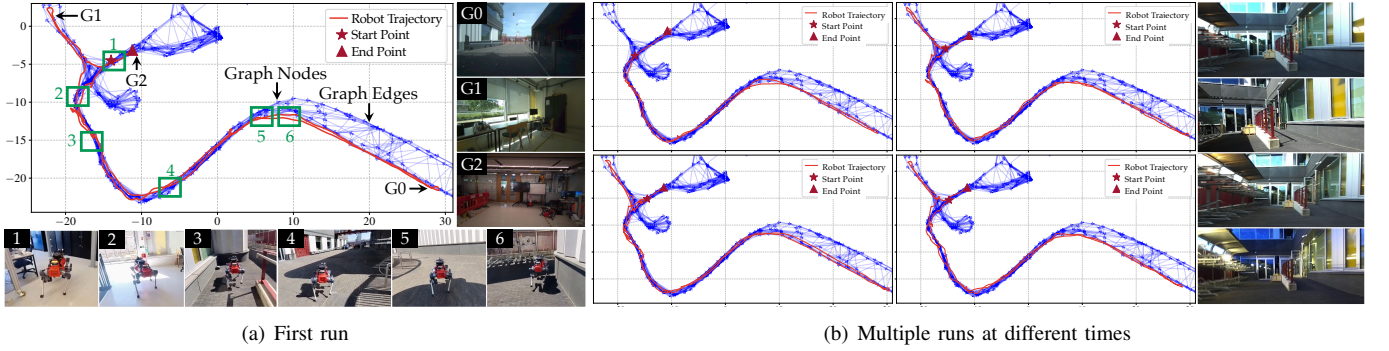


Fig. 18. Real-world experiment (Lab) with a quadruped robot. The topometric map structure comprises nodes (blue arrows) and traversable edges (blue lines). Global planning generates a shortest path on this map to provide subgoals for subsequent motion planning. The red curve denotes the robot's trajectory estimated using our localization method. (a) The robot is sequentially given a set of goal images. It begins inside a room, proceeds outdoors, follows a circular route, and returns to the starting location, covering a total distance of 160m in 312s at an average speed of 0.5m/s. Green boxes labeled 1-6 highlight key planning events: (1 and 2) lab areas, (3) a narrow passageway, (4 and 5) outdoor paths exhibiting varying sunlight conditions, and (6) a right turn facing a wall. (b) The robot is instructed to repeat the navigation task at different times of day, ranging from daytime to nighttime.

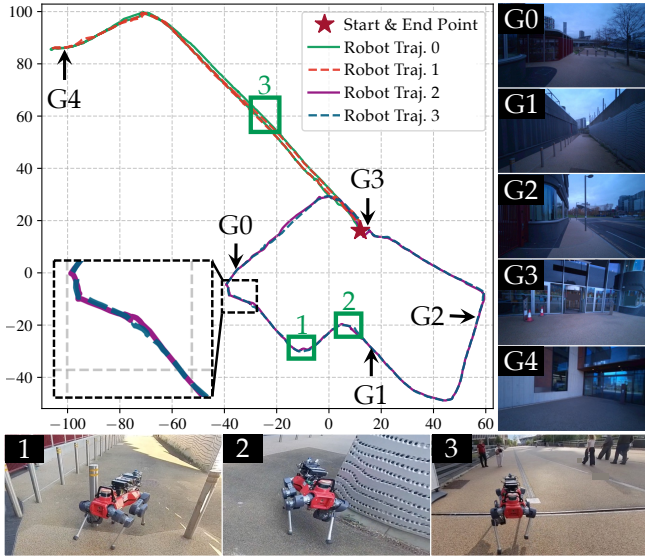


Fig. 19. Real-world experiments (Bridge and Building) demonstrate the robot's capability to autonomously navigate various regions, including a bridge and confined pathways with several obstacles. The robot is given five goal images as visual objectives for its navigation system in Building. Some traverses present shadow-light transition.

ATE and the total node count. Table VII details the ablation study of the culling factors (IQA, IG, and TD) across the pre-filter, forward, and backward stages. The strategy using only IQA achieved the minimum ATE, confirming that IQA effectively removes outlier-prone nodes. The results further indicate that IG and TD as more aggressive culling mechanisms; while they induce a slight trade-off in precision, they enable significant compression. As shown in Fig. 20, the full strategy incorporating all factors reduces map size by approximately 20% with minimal loss in accuracy.

2) *Impact on Visual Localization*: This section validates the necessity of node culling by analyzing its impact on VLoc accuracy. While the primary motivation for culling is storage reduction, arbitrary frame removal risks discarding geometrically critical viewpoints, thereby degrading localization performance. We specifically evaluate how different culling strategies affect metric localization accuracy for the

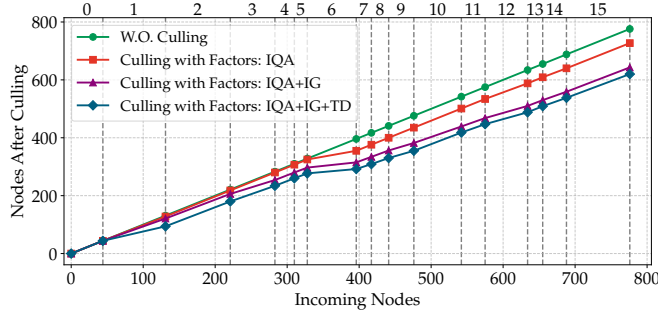
TABLE VII
ABLATION STUDY ON NODE CULLING. IQA: IMAGE QUALITY ASSESSMENT, IG: INFORMATION GAIN, AND TD: TEMPORAL DIFFERENCE.

Operations	Factors	Metrics				
		PreFilter	Forward	Backward	TD	Translational ATE [m]↓
W.O. Node Culling	✗	✗	✗	✗	✗	0.105
Node Culling	✓	✓	✓	✓	✗	0.099
	✓	✓	✓	✓	✗	0.108
	✓	✓	✓	✓	✓	0.116

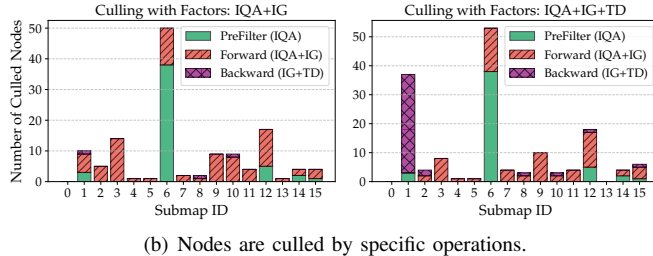
downstream VNav task (Sec. V-A). We exclude image quality and temporal relevance factors, as these attributes exhibit minimal variation within the tested datasets. Instead, we focus the comparative analysis on three distinct culling strategies, where the last is our proposed approach (Sec. IV-D):

- **Pose Density**: A node is culled if its translational and rotational distances to the nearest existing node are below set thresholds. This method is computationally efficient but ignores all visual content.
- **2D Feature Matching**: A node is culled if it shares sufficient 2D inlier LoFTR feature correspondences [79] with its visually closest neighbor.
- **3D Pointmap Overlap (Ours)**: A node is culled due to insufficient information gain relative to its visually most similar neighbor, as detailed in Sec. IV-D.

We use the Map-Free and GZ-Campus datasets for this analysis. For each scene, we apply each culling strategy to select 75% of the images to construct a reference map. The remaining 25% of images are held out and used as query frames for localization. Results, reported as Precision@[25cm, 5°], are summarized in Table VIII. The Pose Density strategy achieves significant map compression, reducing storage by 87.5% (Map-Free) and 75.6% (GZ-Campus). However, this comes at the cost of reduced viewpoint coverage, increasing maximum positional errors by 0.55m. In contrast, both 2D Feature Matching and 3D Pointmap Overlap achieve comparable map compression rates but yield higher localization accuracy and smaller maximum errors than Pose Density. This demonstrates that visually or geometrically informed culling is crucial for preserving localization-critical information.



(a) Evolution of the number of nodes in the map during map merging, where the above number indicates the incoming submap ID.



(b) Nodes are culled by specific operations.

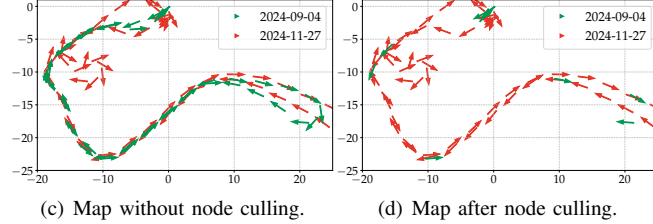


Fig. 20. Lifelong operation for the incremental map merging in Lab, where the dataset spans over three months. Nodes built with two-session maps are shown in (c) and (d), where the arrow direction indicates the forward direction.

We adopt the 3D Pointmap Overlap strategy, as it can effectively reuse immediate results (*i.e.*, the feed-forward pointmap prediction) from the collaborative localization pipeline. We note that any culling strategy inherently risks discarding infrequently observed features, which can increase maximum localization errors. For resource-constrained robots, more adaptive culling strategies may be preferable to better balance computational efficiency with localization robustness.

VIII. DISCUSSION

A. Main Advantages

OPENNAVMAP is a lightweight, extensible, and structure-free topometric map designed for robotic navigation. Each node mainly stores an RGB image to represent the environment, while edges encode odometric, covisibility, and traversability relationships, supporting both metric-level localization and path planning. OPENNAVMAP's primary strengths include: 1) *cross-device multi-session mapping*, integrating submaps from heterogeneous devices captured at varying times and perspectives, thereby enhancing the mapping coverage and update frequency; 2) *robust collaborative localization*, enabled by a coarse-to-fine pipeline with robust outlier rejection that ensures resilience to viewpoint variations, sparse observations, and appearance changes; and 3) *multi-modal extensibility*, nat-

TABLE VIII
POSE ESTIMATION PERFORMANCE WITHIN THE REFERENCE MAP.

Map-Free Dataset ($N_{Query} = 7369$)				
Strategy	Node Number	Maximum $E_t[m]/E_r[deg] \downarrow$	Avg. Median $E_t[m]/E_r[deg] \downarrow$	Precision [%] $[25cm, 5^\circ] \uparrow$
Full KF Set	29629	0.36/6.81	0.006/0.15	99.77
Pose Density	3691	0.91/16.08	0.018/ 0.28	96.40
2D Feature	3803	0.67/ 11.65	0.019/0.30	96.93
3D Pointmap	3961	0.61/11.91	0.017/0.28	97.50

GZ Campus Dataset ($N_{Query} = 476$)				
Strategy	Node Number	Maximum $E_t[m]/E_r[deg] \downarrow$	Avg. Median $E_t[m]/E_r[deg] \downarrow$	Precision [%] $[25cm, 5^\circ] \uparrow$
Full KF Set	1451	1.47/1.65	0.19/0.59	69.54
Pose Density	354	2.05/4.16	0.21/0.74	62.82
2D Feature	720	1.85/2.26	0.19/0.64	69.12
3D Pointmap	720	1.86/ 2.25	0.19/0.64	69.12

urally supporting image-goal navigation and easily adaptable to multi-modal commands.

Unlike conventional topological maps, which are typically limited to path planning, OPENNAVMAP integrates both localization and planning within a unified topometric framework. This capability, combined with support for distributed data collection and multi-session mapping, demonstrates significant potential for scalable, real-world deployment. Nevertheless, the current implementation relies on a computationally intensive 3D GFM for online pointmap generation and optimization. Future improvements to inference speed (*e.g.*, via network quantization and pruning) are needed to enhance computational efficiency and practical applicability.

B. Limitations and Future Works

We further indicate several directions for future research beyond the proposed OPENNAVMAP:

- *Sequence-Based Matching*: While our current DP-based sequence matching effectively leverages temporal continuity, its reliance on traversal sequences for indexing, rather than the underlying graph topology, limits its flexibility. Furthermore, exhaustive traversal searches are computationally inefficient in large-scale mapping scenarios. Future research should explore hierarchical, graph-based [80], or location-indexed strategies to exploit the inherent graph topology, enabling more flexible and efficient matching of image sets (*e.g.*, nearby, non-sequential images).
- *Generalization of 3D Foundation Models*: Although we demonstrate strong generalization by directly deploying state-of-the-art 3D GFMs without retraining, performance degradation persists under significant cross-device variations, illumination shifts, and dynamic environmental changes. As noted in [49], the cross-device domain gap is notably more challenging than single-device scenarios. Consequently, developing increasingly generalizable 3D GFMs [5], [81] remains a critical research direction for addressing these robustness issues.
- *Centralized Multi-Session Mapping*: The current centralized mapping framework suffers from scalability limitations in large-scale, multi-device, crowd-sourced contexts, leading to computational, storage, and communica-

cation bottlenecks. Developing decentralized collaborative mapping frameworks, potentially using Gaussian belief propagation (GBP) [82] and distributed optimization, could significantly enhance scalability, real-time performance, and adaptability for large-scale deployment.

- *Conservative Node Culling*: Our culling approach is currently conservative. Ideally, the number of retained nodes should scale primarily with environmental complexity rather than traversal frequency. Future research should explore more aggressive and adaptive culling methods to effectively reduce redundancy without compromising localization accuracy.
- *Navigation and Out-of-Map Recovery*: The current VNav assumes operation strictly within known map boundaries, lacking robust recovery mechanisms for out-of-map scenarios (e.g., robot kidnapping). Integrating autonomous exploration and active SLAM methodologies in future systems would allow robots to recover from unfamiliar or incorrect initialization conditions, thereby significantly improving operational autonomy and robustness.

IX. CONCLUSION

In this work, we introduced OPENNAVMAP, a visual collaborative localization and multi-session mapping system designed for scalability. By leveraging a lightweight, structure-free topometric representation and a 3D GFM, our approach addresses key challenges in long-term navigation. The introduction of GV and CCM modules ensures robustness by effectively filtering false positives. Through extensive experiments in diverse indoor and urban environments, OPENNAVMAP demonstrated superior performance compared to structure-based methods such as HLoc, especially under large viewpoint variations. Crucially, our results show that despite its lightweight nature, the proposed map supports sub-meter accuracy for localization and planning. This was validated through 12 successful autonomous navigation trials on mobile platforms in both simulation and the real world. These findings validate our central hypothesis: sparse observational maps can match or exceed the performance of globally consistent 3D models while drastically reducing computational and construction complexity. We will make our source code and datasets publicly available to support the community.

ACKNOWLEDGMENT

The authors would like to express their sincere gratitude to Dr. Shuyang Zhang and Dr. Yilong Zhu for their valuable suggestions on visual mapping and data collection, and to Dr. Sajad Saedi for insightful discussions on collaborative localization and map merging. The authors also thank ANYbotics for their assistance with robot maintenance, and gratefully acknowledge the use of AI tools in refining the manuscript.

REFERENCES

- [1] X. Pan, G. Huang, Z. Zhang, J. Li, H. Bao, and G. Zhang, “Robust collaborative visual-inertial slam for mobile augmented reality,” *IEEE Trans. Vis. Comput. Graph.*, 2024.
- [2] E. Arnold, J. Wynn, S. Vicente, G. Garcia-Hernando, A. Monszpart, V. Prisacariu, D. Turmukhambetov, and E. Brachmann, “Map-free visual relocalization: Metric pose relative to a single image,” in *Proc. Eur. Conf. Comput. Vis.*, 2022, pp. 690–708.
- [3] V. Leroy, Y. Cabon, and J. Revaud, “Grounding image matching in 3D with MAS3R,” in *Proc. Eur. Conf. Comput. Vis.*, 2024, pp. 71–91.
- [4] S. Wang, V. Leroy, Y. Cabon, B. Chidlovskii, and J. Revaud, “DUST3R: Geometric 3D vision made easy,” in *Proc. IEEE/CVF Conf. Comput. Vis. Pattern Recognit.*, 2024, pp. 20697–20709.
- [5] J. Wang, M. Chen, N. Karaev, A. Vedaldi, C. Rupprecht, and D. Novotny, “VGGT: Visual geometry grounded transformer,” in *Proc. IEEE/CVF Conf. Comput. Vis. Pattern Recognit.*, 2025, pp. 5294–5306.
- [6] J. Lee, M. Bjelonic, A. Reske, L. Wellhausen, T. Miki, and M. Hutter, “Learning robust autonomous navigation and locomotion for wheeled-legged robots,” *Sci. Robot.*, vol. 9, no. 89, p. eadi9641, 2024.
- [7] W. Maddern, G. Pascoe, C. Linegar, and P. Newman, “1 year, 1000 km: The oxford robotcar dataset,” *Int. J. Robot. Res.*, vol. 36, no. 1, pp. 3–15, 2017.
- [8] J. L. Schönberger and J.-M. Frahm, “Structure-from-motion revisited,” in *Proc. IEEE/CVF Conf. Comput. Vis. Pattern Recognit.*, 2016.
- [9] T. Qin, C. Li, H. Ye, S. Wan, M. Li, H. Liu, and M. Yang, “Crowdsourced NeRF: Collecting data from production vehicles for 3D street view reconstruction,” *IEEE Trans. Intell. Transp. Syst.*, 2024.
- [10] OpenStreetMap contributors, “Planet dump retrieved from <https://planet.osm.org/>,” <https://www.openstreetmap.org/>, 2017.
- [11] D. Anguelov, C. Dulong, D. Filip, C. Frueh, S. Lafon, R. Lyon, A. Ogale, L. Vincent, and J. Weaver, “Google street view: Capturing the world at street level,” *IEEE Computer*, vol. 43, no. 6, pp. 32–38, 2010.
- [12] P.-E. Sarlin, D. DeTone, T.-Y. Yang, A. Avetisyan, J. Straub, T. Malisiewicz, S. R. Bulo, R. Newcombe, P. Kotschieder, and V. Balntas, “OrienterNet: Visual localization in 2D public maps with neural matching,” in *Proc. IEEE/CVF Conf. Comput. Vis. Pattern Recognit.*, 2023, pp. 21632–21642.
- [13] P. Yin, J. Jiao, S. Zhao, L. Xu, G. Huang, H. Choset, S. Scherer, and J. Han, “General place recognition survey: Towards real-world autonomy,” *IEEE Trans. Robot.*, 2025.
- [14] J. Jiao, J. He, C. Liu, S. Aegidius, X. Hu, T. Braud, and D. Kanoulas, “LiteVLoc: Map-lite visual localization for image goal navigation,” in *Proc. IEEE Int. Conf. Robot. Autom.*, 2025.
- [15] N. Hughes, Y. Chang, and L. Carlone, “Hydra: A real-time spatial perception system for 3D scene graph construction and optimization,” *arXiv preprint arXiv:2201.13360*, 2022.
- [16] P. Furgale and T. D. Barfoot, “Visual teach and repeat for long-range rover autonomy,” *J. Field Robot.*, vol. 27, no. 5, pp. 534–560, 2010.
- [17] J. Engel *et al.*, “Project Aria: A new tool for egocentric multi-modal ai research,” *arXiv preprint arXiv:2308.13561*, 2023.
- [18] L. Carlone, A. Kim, F. Dellaert, T. Barfoot, and D. Cremers, *SLAM Handbook. From Localization and Mapping to Spatial Intelligence*, L. Carlone, A. Kim, F. Dellaert, T. Barfoot, and D. Cremers, Eds. Cambridge University Press, 2024.
- [19] R. Mur-Artal, J. M. M. Montiel, and J. D. Tardos, “ORB-SLAM: A versatile and accurate monocular SLAM system,” *IEEE Trans. Robot.*, vol. 31, no. 5, pp. 1147–1163, 2015.
- [20] C. Zheng, W. Xu, Z. Zou, T. Hua, C. Yuan, D. He, B. Zhou, Z. Liu, J. Lin, F. Zhu *et al.*, “Fast-LIVO2: Fast, direct lidar-inertial-visual odometry,” *IEEE Trans. Robot.*, 2024.
- [21] B. Kerbl, G. Kopanas, T. Leimkühler, and G. Drettakis, “3D gaussian splatting for real-time radiance field rendering,” *ACM Trans. Graph.*, vol. 42, no. 4, pp. 1–14, 2023.
- [22] T. Dang, M. Tranzatto, S. Khattak, F. Mascarich, K. Alexis, and M. Hutter, “Graph-based subterranean exploration path planning using aerial and legged robots,” *J. Field Robot.*, vol. 37, no. 8, pp. 1363–1388, 2020.
- [23] G. Berton, C. Masone, and B. Caputo, “Rethinking visual geolocation for large-scale applications,” in *Proc. IEEE/CVF Conf. Comput. Vis. Pattern Recognit.*, 2022, pp. 4878–4888.
- [24] D. Shah, A. Sridhar, A. Bhorkar, N. Hirose, and S. Levine, “GNM: A general navigation model to drive any robot,” in *Proc. IEEE Int. Conf. Robot. Autom.*, 2023, pp. 7226–7233.
- [25] R. Martin-Brualla, N. Radwan, M. S. Sajjadi, J. T. Barron, A. Dosovitskiy, and D. Duckworth, “NeRF in the wild: Neural radiance fields for unconstrained photo collections,” in *Proc. IEEE/CVF Conf. Comput. Vis. Pattern Recognit.*, 2021, pp. 7210–7219.
- [26] E. Brachmann, T. Cavallari, and V. A. Prisacariu, “Accelerated coordinate encoding: Learning to relocalize in minutes using RGB and poses,” in *Proc. IEEE/CVF Conf. Comput. Vis. Pattern Recognit.*, 2023, pp. 5044–5053.

[27] M. Adamkiewicz, T. Chen, A. Caccavale, R. Gardner, P. Culbertson, J. Bohg, and M. Schwager, “Vision-only robot navigation in a neural radiance world,” *IEEE Robot. Autom. Lett.*, vol. 7, no. 2, pp. 4606–4613, 2022.

[28] A. Rosinol, A. Violette, M. Abate, N. Hughes, Y. Chang, J. Shi, A. Gupta, and L. Carlone, “Kimera: From SLAM to spatial perception with 3D dynamic scene graphs,” *Int. J. Robot. Res.*, vol. 40, no. 12-14, pp. 1510–1546, 2021.

[29] H. Bavle, J. L. Sanchez-Lopez, M. Shaheer, J. Civera, and H. Voos, “S-graphs+: Real-time localization and mapping leveraging hierarchical representations,” *IEEE Robot. Autom. Lett.*, vol. 8, no. 8, pp. 4927–4934, 2023.

[30] M. Paton, K. MacTavish, M. Warren, and T. D. Barfoot, “Bridging the appearance gap: Multi-experience localization for long-term visual teach and repeat,” in *Proc. IEEE/RSJ Int. Conf. Intell. Robots Syst.*, 2016, pp. 1918–1925.

[31] W. Churchill and P. Newman, “Experience-based navigation for long-term localisation,” *Int. J. Robot. Res.*, vol. 32, no. 14, pp. 1645–1661, 2013.

[32] D. Gálvez-López and J. D. Tardos, “Bags of binary words for fast place recognition in image sequences,” *IEEE Trans. Robot.*, vol. 28, no. 5, pp. 1188–1197, 2012.

[33] R. Arandjelović, P. Gronát, A. Torii, T. Pajdla, and J. Sivic, “NetVLAD: CNN architecture for weakly supervised place recognition,” in *Proc. IEEE/CVF Conf. Comput. Vis. Pattern Recognit.*, 2016, pp. 5297–5307.

[34] M. J. Milford and G. F. Wyeth, “SeqSLAM: Visual route-based navigation for sunny summer days and stormy winter nights,” in *Proc. IEEE Int. Conf. Robot. Autom.*, 2012, pp. 1643–1649.

[35] O. Vysotska and C. Stachniss, “Lazy data association for image sequences matching under substantial appearance changes,” *IEEE Robot. Autom. Lett.*, vol. 1, no. 1, pp. 213–220, 2015.

[36] S. Garg and M. Milford, “SeqNet: Learning descriptors for sequence-based hierarchical place recognition,” *IEEE Robot. Autom. Lett.*, vol. 6, no. 3, pp. 4305–4312, 2021.

[37] P.-Y. Lajoie, S. Hu, G. Beltrame, and L. Carlone, “Modeling perceptual aliasing in slam via discrete-continuous graphical models,” *IEEE Robot. Autom. Lett.*, vol. 4, no. 2, pp. 1232–1239, 2019.

[38] X. Liu, J. Lei, A. Prabhu, Y. Tao, I. Spasojevic, P. Chaudhari, N. Atanasov, and V. Kumar, “SlideSLAM: Sparse, lightweight, decentralized metric-semantic slam for multi-robot navigation,” *arXiv preprint arXiv:2406.17249*, 2024.

[39] Y. Tian, Y. Chang, F. H. Arias, C. Nieto-Granda, J. P. How, and L. Carlone, “Kimera-Multi: Robust, distributed, dense metric-semantic slam for multi-robot systems,” *IEEE Trans. Robot.*, vol. 38, no. 4, 2022.

[40] X. Gao, X. Hou, J. Tang, and H.-F. Cheng, “Complete solution classification for the perspective-three-point problem,” *IEEE Trans. Pattern Anal. Mach. Intell.*, vol. 25, pp. 930–943, 2003.

[41] M. A. Fischler and R. C. Bolles, “Random sample consensus: a paradigm for model fitting with applications to image analysis and automated cartography,” *Commun. ACM*, vol. 24, no. 6, pp. 381–395, 1981.

[42] L. Lipson and J. Deng, “Multi-session slam with differentiable wide-baseline pose optimization,” in *Proc. IEEE/CVF Conf. Comput. Vis. Pattern Recognit.*, 2024, pp. 19626–19635.

[43] M. Karrer, P. Schmuck, and M. Chli, “CVI-SLAM—collaborative visual-inertial SLAM,” *IEEE Robot. Autom. Lett.*, vol. 3, no. 4, pp. 2762–2769, 2018.

[44] H. Xu, P. Liu, X. Chen, and S. Shen, “D2SLAM: Decentralized and distributed collaborative visual-inertial SLAM system for aerial swarm,” *IEEE Trans. Robot.*, 2024.

[45] A. Kendall, M. Grimes, and R. Cipolla, “PoseNet: A convolutional network for real-time 6-dof camera relocalization,” in *Proc. IEEE/CVF Int. Conf. Comput. Vis.*, 2015, pp. 2938–2946.

[46] X. Jiang, F. Wang, S. Galliani, C. Vogel, and M. Pollefeys, “R-SCoRe: Revisiting scene coordinate regression for robust large-scale visual localization,” in *Proc. IEEE/CVF Conf. Comput. Vis. Pattern Recognit.*, 2025.

[47] P.-E. Sarlin, M. Dusmanu, J. L. Schönberger, P. Speciale, L. Gruber, V. Larsson, O. Miksik, and M. Pollefeys, “LaMAR: Benchmarking localization and mapping for augmented reality,” in *Proc. Eur. Conf. Comput. Vis.*, 2022, pp. 686–704.

[48] H. Wei, J. Jiao, X. Hu, J. Yu, X. Xie, J. Wu, Y. Zhu, Y. Liu, L. Wang, and M. Liu, “FusionPortableV2: A unified multi-sensor dataset for generalized SLAM across diverse platforms and scalable environments,” *Int. J. Robot. Res.*, p. 02783649241303525, 2024.

[49] H. Blum, A. Mercurio, J. O'Reilly, T. Engelbracht, M. Dusmanu, M. Pollefeys, and Z. Bauer, “CroCoDL: Cross-device collaborative dataset for localization,” in *Proc. IEEE/CVF Conf. Comput. Vis. Pattern Recognit.*, 2025, pp. 27424–27434.

[50] H. Huang, C. Liu, Y. Zhu, H. Cheng, T. Braud, and S.-K. Yeung, “360Loc: A dataset and benchmark for omnidirectional visual localization with cross-device queries,” in *Proc. IEEE/CVF Conf. Comput. Vis. Pattern Recognit.*, 2024, pp. 22314–22324.

[51] Ö. Tuzcuoğlu, A. Köksal, B. Sofu, S. Kalkan, and A. A. Alatan, “Xoftr: Cross-modal feature matching transformer,” in *Proc. IEEE/CVF Conf. Comput. Vis. Pattern Recognit.*, 2024, pp. 4275–4286.

[52] X. He, H. Yu, S. Peng, D. Tan, Z. Shen, H. Bao, and X. Zhou, “Matchanything: Universal cross-modality image matching with large-scale pre-training,” *arXiv preprint arXiv:2501.07556*, 2025.

[53] Z. Lu, H. Yang, D. Xu, B. Li, B. Ivanovic, M. Pavone, and Y. Wang, “LoRA3D: Low-rank self-calibration of 3D geometric foundation models,” in *Int. Conf. Learn. Represent.*, 2025.

[54] J. Yu, H. Ye, J. Jiao, P. Tan, and H. Zhang, “GV-Bench: Benchmarking local feature matching for geometric verification of long-term loop closure detection,” in *Proc. IEEE/RSJ Int. Conf. Intell. Robots Syst.*, 2024, pp. 7922–7928.

[55] P.-E. Sarlin, C. Cadena, R. Siegwart, and M. Dymczyk, “From coarse to fine: Robust hierarchical localization at large scale,” in *Proc. IEEE/CVF Conf. Comput. Vis. Pattern Recognit.*, 2019.

[56] F. Dellaert and G. Contributors, “borglab/gtsam,” 2022. [Online]. Available: <https://github.com/borglab/gtsam>

[57] J. Ke, Q. Wang, Y. Wang, P. Milanfar, and F. Yang, “MUSIQ: Multi-scale image quality transformer,” in *Proc. IEEE/CVF Int. Conf. Comput. Vis.*, 2021, pp. 5148–5157.

[58] Z. Yu, Z. Qiao, W. Liu, H. Yin, and S. Shen, “SLiM: Scalable and lightweight lidar mapping in urban environments,” *IEEE Trans. Robot.*, 2025.

[59] T. Qin, P. Li, and S. Shen, “VINS-Mono: A robust and versatile monocular visual-inertial state estimator,” *IEEE Trans. Robot.*, vol. 34, no. 4, pp. 1004–1020, 2018.

[60] X. Hu, J. Wu, J. Jiao, W. Zhang, and P. Tan, “MS-Mapping: Multi-session lidar mapping with wasserstein-based keyframe selection,” *arXiv preprint arXiv:2406.02096*, 2024.

[61] S. Ågëdius, D. Hadjivelichkov, J. Jiao, J. Embley-Riches, and D. Kanoulas, “Watch your STEPP: Semantic traversability estimation using pose projected features,” in *Proc. IEEE Int. Conf. Robot. Autom.*, 2025, pp. 2376–2382.

[62] G. Berton, G. Trivigno, B. Caputo, and C. Masone, “EigenPlaces: Training viewpoint robust models for visual place recognition,” in *Proc. IEEE/CVF Int. Conf. Comput. Vis.*, 2023, pp. 11080–11090.

[63] N. Keetha, A. Mishra, J. Karhade, K. M. Jatavallabhula, S. Scherer, M. Krishna, and S. Garg, “AnyLoc: Towards universal visual place recognition,” *IEEE Robot. Autom. Lett.*, vol. 9, no. 2, pp. 1286–1293, 2023.

[64] G. Berton and C. Masone, “Megaloc: One retrieval to place them all,” in *Proc. IEEE/CVF Conf. Comput. Vis. Pattern Recognit.*, 2025, pp. 2861–2867.

[65] J. Zhang, C. Hu, R. G. Chadha, and S. Singh, “Falco: Fast likelihood-based collision avoidance with extension to human-guided navigation,” *J. Field Robot.*, vol. 37, no. 8, pp. 1300–1313, 2020.

[66] A. Chang, A. Dai, T. Funkhouser, M. Halber, M. Niebner, M. Savva, S. Song, A. Zeng, and Y. Zhang, “Matterport3D: Learning from RGB-D data in indoor environments,” in *Proc. Int. Conf. 3D Vis.*, 2017, pp. 667–676.

[67] F. Yang, C. Wang, C. Cadena, and M. Hutter, “iPlanner: Imperative path planning,” *arXiv preprint arXiv:2302.11434*, 2023.

[68] M. Bloesch, “State estimation for legged robots-kinematics, inertial sensing, and computer vision,” Ph.D. dissertation, ETH Zurich, 2017.

[69] A. Krishnan, S. Liu, P.-E. Sarlin, O. Gentilhomme, D. Caruso, M. Monge, R. Newcombe, J. Engel, and M. Pollefeys, “Benchmarking egocentric visual-inertial SLAM at city scale,” in *Proc. IEEE/CVF Int. Conf. Comput. Vis.*, 2025, pp. 25207–25217.

[70] C. Liu, Y. Zhao, and T. Braud, “MARViN: Mobile AR dataset with visual-inertial data,” in *Proc. IEEE Conf. Virtual Real. 3D User Interfaces Abstr. Workshops*, 2024, pp. 532–538.

[71] J. Jiao *et al.*, “Supplementary Materials of OpenNavMap: Structure-Free Topometric Mapping via Large-Scale Collaborative Localization,” 2025.

[72] Z. Zhang and D. Scaramuzza, “A tutorial on quantitative trajectory evaluation for visual (-inertial) odometry,” in *Proc. IEEE/RSJ Int. Conf. Intell. Robots Syst.*, 2018, pp. 7244–7251.

[73] A. Gordo, J. Almazan, J. Revaud, and D. Larlus, “End-to-end learning of deep visual representations for image retrieval,” *Int. J. Comput. Vis.*, vol. 124, no. 2, pp. 237–254, 2017.

- [74] M. Tyszkiewicz, P. Fua, and E. Trulls, “DISK: Learning local features with policy gradient,” in *Adv. Neural Inf. Process. Syst.*, vol. 33, 2020, pp. 14 254–14 265.
- [75] D. DeTone, T. Malisiewicz, and A. Rabinovich, “SuperPoint: Self-supervised interest point detection and description,” in *Proc. IEEE Conf. Comput. Vis. Pattern Recognit. Workshops*, 2018, pp. 224–236.
- [76] P. Lindenberger, P.-E. Sarlin, and M. Pollefeys, “LightGlue: Local feature matching at light speed,” in *Proc. IEEE/CVF Int. Conf. Comput. Vis.*, 2023, pp. 17 627–17 638.
- [77] S. Dong, S. Wang, S. Liu, L. Cai, Q. Fan, J. Kannala, and Y. Yang, “Reloc3r: Large-scale training of relative camera pose regression for generalizable, fast, and accurate visual localization,” in *Proc. IEEE/CVF Conf. Comput. Vis. Pattern Recognit.*, 2025, pp. 16 739–16 752.
- [78] Z. Tang, Y. Fan, D. Wang, H. Xu, R. Ranjan, A. Schwing, and Z. Yan, “MV-Dust3r+: Single-stage scene reconstruction from sparse views in 2 seconds,” in *Proc. IEEE/CVF Conf. Comput. Vis. Pattern Recognit.*, 2025, pp. 5283–5293.
- [79] J. Sun, Z. Shen, Y. Wang, H. Bao, and X. Zhou, “LoFTR: Detector-free local feature matching with transformers,” in *Proc. IEEE/CVF Conf. Comput. Vis. Pattern Recognit.*, 2021, pp. 8922–8931.
- [80] Y. Miao, F. Engelmann, O. Vysotska, F. Tombari, M. Pollefeys, and D. B. Baráth, “SceneGraphLoc: Cross-modal coarse visual localization on 3D scene graphs,” in *Proc. Eur. Conf. Comput. Vis.*, 2024, pp. 127–150.
- [81] H. Lin, S. Chen, J. Liew, D. Y. Chen, Z. Li, G. Shi, J. Feng, and B. Kang, “Depth Anything 3: Recovering the visual space from any views,” *arXiv preprint arXiv:2511.10647*, 2025.
- [82] J. Ortiz, T. Evans, and A. J. Davison, “A visual introduction to gaussian belief propagation,” *arXiv preprint arXiv:2107.02308*, 2021.